NACA RM L56L18

RESEARCH MEMORANDUM

FREE-FLIGHT EXPERIENCE OF THE LATERAL STABILITY CHARACTERISTICS AT LOW LIFT OF A 45° SWEPT-WING ROCKET-PROPELLED MODEL EQUIPPED WITH A NONLINEAR YAW-RATE DAMPER SYSTEM AT MACH NUMBERS FROM 0.76 TO 1.73

By Charles T. D'Aiutolo, William W. Willoughby, and Lucille C. Coltrane

Langley Aeronautical Laboratory
Langley Field, Va.

NATIONAL ADVISORY COMMITTEE FOR AERONAUTICS

WASHINGTON

February 8, 1957
Declassified February 10, 1959

NACA RM L56L18

NATIONAL ADVISORY COMMITTEE FOR AERONAUTICS

RESEARCH MEMORANDUM

FREE-FLIGHT EXPERIENCE OF THE LATERAL STABILITY CHARACTERISTICS AT LOW LIFT OF A 45° SWEPT-WING ROCKET-PROPELLED MODEL EQUIPPED WITH A NONLINEAR YAW-RATE DAMPER SYSTEM AT MACH NUMBERS FROM 0.76 TO 1.73

By Charles T. D'Aiutolo, William W. Willoughby,
and Lucille C. Coltrane

SUMMARY

A low-lift lateral stability investigation was conducted with a rocket-propelled model of a 45° swept-wing-airplane configuration equipped with an auxiliary yaw-rate damper system in the Mach number range from 0.76 to 1.73. The lateral oscillations due to periodic yawing disturbances were analyzed to determine the lateral characteristics of the airframe—yaw-rate-damper combination. In addition, due to a dead spot in the operation of the yaw-rate damper system, it was possible to determine the lateral derivatives of the model when the Mach number was greater than 1.2 by the use of the time-vector method while the damper was essentially inoperative. The data were further interpreted in terms of full-scale-airplane flying qualities.

The yaw-rate damper system was nonlinear due to a relatively large dead spot in the system. The effect of the yaw-rate damper system, where data were available (Mach number greater that 1.2), was to increase the damping of the lateral oscillations. The periods of the lateral oscillations were unaffected by the yaw-rate damper system. When interpreted in terms of full-scale flying qualities, the yaw-rate damper system had a large effect on the damping at a Mach number of 1.4.

INTRODUCTION

Current design trends in airplane geometry and mass distribution have caused serious adverse effects upon the damping of lateral oscillations. As a result, auxiliary systems to improve the damping of

lateral oscillation are being incorporated in high-performance airplanes. Many auxiliary systems have been proposed (for example, see ref. 1) and one which has received widespread use applies rudder control proportional to yawing angular velocity (see, for example, refs. 2 and 3).

In order to provide some additional experience with model testing of automatic controls and to provide further information on the effect of an auxiliary yaw damper sensitive to yawing angular velocity on the lateral stability of high-performance airplanes, a rocket-propelled model of a 45° swept-wing airplane equipped with an auxiliary yaw-rate damper system similar to the system tested in reference 4 was flown at transonic and supersonic speeds. The yaw-rate damper system was linked to an all-movable vertical tail which deflected as a function of the yawing velocities caused by periodic yawing disturbances. The Mach number range covered by this test was from 0.76 to 1.73 and corresponds to a Reynolds number range (based on wing mean aerodynamic chord) of 6.9×10^6 to 16.2×10^6, respectively. The model was flown at the Langley Pilotless Aircraft Research Station at Wallops Island, Va.

Due to a dead spot in the operation of the yaw-rate damper system, it was possible to obtain the lateral stability derivatives of the airplane while the system was essentially inoperative. The lateral stability derivatives were obtained by use of the time-vector method as applied to rocket-propelled models as described in references 5, 6, and 7.

SYMBOLS AND COEFFICIENTS

The forces and moments acting on the model are referred to the body system of axes shown in figure 1. The origin of the axes system was at the center of gravity of the model which was coincident with the 25-percent mean aerodynamic chord of the wing. The symbols and coefficients are defined as follows:

a	total damping factor (logarithmic decrement of the Dutch roll oscillation defined as being a positive number for a damped oscillation)
$A_{Y/g}$	acceleration along Y reference axis as obtained from accelerometer, positive to right
b	wing span, ft
$\bar{c}$	mean aerodynamic chord, ft

$c_{1/2}$	number of cycles required for oscillation to damp to 1/2 amplitude
h	altitude, ft
I_X	moment of inertia about X-axis, slug-ft^2
I_Z	moment of inertia about Z-axis, slug-ft^2
I_{XZ}	product of inertia in XZ-plane referred to body axes system (positive when the positive direction of the X principal axis is inclined below the reference axis), $1/2 \left(I_Z - I_X\right) \tan 2\epsilon$, slug-ft^2
L	concentrated load, lb
M	Mach number
M_X, M_Y, M_Z	rolling, pitching, and yawing moments about X-, Y-, and Z-axes, respectively
m	mass, slugs
P	period of lateral oscillation, sec
p	rolling velocity, radians per second
q	dynamic pressure, lb/sq ft
R	Reynolds number
r	yawing velocity, radians per second
S	total wing area, sq ft
$T_{1/2}$	time required for the lateral oscillation to damp to 1/2 amplitude, sec
V	velocity, ft/sec
V_e	equivalent airspeed, $V\sqrt{\sigma}$, ft/sec
v_e	equivalent lateral velocity, $V_e \sin \beta$, ft/sec
W	weight of model, lb
X,Y,Z	coordinate axes

y	spanwise station, ft
y'	spanwise station at which concentrated load is applied, ft
α	angle of attack, deg or radians as noted
β	angle of sideslip, deg or radians as noted
ϵ	principal-axis inclination, deg
$\eta = \frac{y}{b/2}$	
σ	density ratio
θ	angle of twist or pitch angle, radians
μ	relative-density factor, $\frac{m}{\rho S b}$
ρ	air density, slugs/cu ft
ϕ	roll angle, radians
ψ	yaw angle, radians
Φ	phase angle, deg
δ	control deflection, deg
ζ	critical damping ratio
ω_n	undamped natural frequency of the model, radians/sec
ω	undamped natural frequency of the yaw damper system, radians/sec
C_Y	lateral-force coefficient, Lateral force/qS
C_n	yawing-moment coefficient, Yawing moment/qSb
C_L	lift coefficient, $\frac{\text{Lift}}{qS}$
C_l	rolling-moment coefficient, Rolling moment/qSb

C_{Y_β} lateral-force derivative, $\partial C_Y/\partial\beta$, per radian

C_{n_β} directional-stability derivative, $\partial C_n/\partial\beta$, per radian

C_{l_β} effective-dihedral derivative, $\partial C_l/\partial\beta$, per radian

C_{l_p} damping-in-roll derivative, $\frac{\partial C_l}{\partial \frac{pb}{2V}}$, per radian

C_{n_r} rate of change of yawing-moment coefficient with yawing-angular-velocity factor, $\frac{\partial C_n}{\partial \frac{rb}{2V}}$, per radian

$C_{n_{\dot\beta}}$ rate of change of yawing-moment coefficient with rate of change of angle-of-sideslip factor, $\frac{\partial C_n}{\partial \frac{\dot\beta b}{2V}}$, per radian

C_{n_p} rate of change of yawing-moment coefficient with rolling-angular-velocity factor, $\frac{\partial C_n}{\partial \frac{pb}{2V}}$, per radian

C_{l_r} rate of change of rolling-moment coefficient with yawing-angular-velocity factor, $\frac{\partial C_l}{\partial \frac{rb}{2V}}$, per radian

Subscripts:

w wing

T trim

HT horizontal tail

t vertical tail

A full-scale airplane

The symbol | | represents the absolute magnitude of the amplitude of a quantity and is always taken to be positive. A dot over a variable indicates the first derivative of the variable with respect to time. Two dots indicate the second derivative with respect to time. The second subscript symbol of the phase angles is used as a reference. A positive sign associated with the phase angle indicates that the first subscript symbol leads the reference, whereas a negative sign indicates that the first subscript symbol lags the reference.

MODEL, INSTRUMENTATION, AND TESTS

Model

The general arrangement of the model is shown in figure 2, and the geometric characteristics of the model are presented in table I. In table II the mass and inertia characteristics of the model are listed. Photographs of the model and model-booster combination are presented as figure 3.

The fuselage was a body of revolution and consisted of an ogival nose section, a cylindrical body section, and an ogival tail section. The nose section contained the electrically actuated yaw-vane disturber and the telemeter; the center section contained the wing, and the tail section contained the horizontal and vertical tails as well as the auxiliary yaw damper system. The fuselage was constructed of aluminum alloy with magnesium skin.

The wing of the model was mounted along the fuselage reference line and was constructed of composite wood and steel. It incorporated 45° of sweepback along the quarter-chord line and had an aspect ratio of 4 and a taper ratio of 0.3. The airfoil sections were NACA 65A006. The horizontal tail was mounted in the wing-chord plane extended and had the same geometrical characteristics as those of the wing. It was constructed of solid steel.

The vertical tail had an NACA 65A006 airfoil section and incorporated 45° of sweepback along the quarter-chord line (see table I for other geometric characteristics). It was constructed of solid steel and was mounted through linkages to the auxiliary yaw damper.

The yaw-rate damper system consisted of a rate gyroscope, pneumatic servomotor, slide valve, air accumulator, air regulator, air purifier, and linkages. Rate-gyro signals were transmitted by mechanical linkages through the air valves and servomotor to produce deflections of the movable vertical tail. The mechanical linkage limited the vertical

tail to maximum deflection of ±7°. A complete description of the auxiliary yaw damper system is presented in the appendix.

Instrumentation

The model contained a standard NACA eight-channel telemeter. Continuous measurements of the following quantities were recorded: Normal and transverse accelerations near the center of gravity of the model, rolling and yawing velocities, angles of attack and sideslip, total pressure, and vertical-tail deflection. Rolling velocity was measured by means of a gyro-type instrument alined so that it was sensitive to velocities about the X reference axis and yaw velocity was measured by a similar instrument alined so that it was sensitive to velocities about the Z reference axis. The angle of attack and angle of sideslip were measured by an air-flow direction indicator located on a sting forward of the model. Total pressure was measured by a tube located on a strut attached to the under side of the cylindrical section of the fuselage and the vertical-tail deflection was measured by an inductance-type control position indicator mounted to a shaft that formed the hinge line of the vertical tail.

Ground instrumentation included a CW Dopplar radar unit to measure the velocity of the model, a modified SCR-584 tracking radar set to measure the positions of the model in space, and a spinsonde used as an additional measure of the rolling velocity by means of the polarized radio waves emanating from the telemeter antenna. Atmospheric data were obtained from a radiosonde released immediately before model flight, and fixed and tracking motion-picture cameras were used to observe the condition of the model during most of the flight.

Preflight Tests

The stiffness of the wing was obtained by applying concentrated static loads at five spanwise stations along the quarter-chord and half-chord lines and measuring the deflections along the leading and trailing edges. The stiffness of the vertical tail was obtained in a similar manner but four spanwise stations were used for the concentrated static loads due to the space requirements of the dials used to measure the leading- and trailing-edge deflections. These data are shown in figure 4.

The moments of inertia of the model were obtained by swinging the model as a pendulum and measuring the frequency of the oscillations. The inclination of the principal axis of inertia was obtained by swinging the model in roll about a number of longitudinal-axis inclinations and noting the angle for which the roll moment of inertia was a minimum.

The model was also suspended by shock chords and shaken by means of an electromagnetic shaker to obtain its structural natural frequencies. These characteristics are shown in table II.

Flight Test

The model was boosted to a Mach number of 1.76 by two solid-fuel ABL Deacon rocket motors which were timed to fire simultaneously, and upon burnout of the booster rocket motors the model separated from the booster as a result of the different drag-to-weight ratios. The model did not contain an internal rocket motor. During the boosted phase of the flight, the yaw-vane disturber was inoperative and was not allowed to operate until the model was completely separated from the booster. No such restriction was placed on the auxiliary yaw damper system, however, and the vertical tail was allowed to move during boosted flight. After completely separating from the booster, the yaw-vane disturber was programmed to extend fully in a time of 0.38 second and to retract in a time of approximately 0.05 second, repeating the cycle every 1.43 seconds. Since the yaw vanes were set at a fixed angle of 10° with respect to the model fuselage center line, the model assumed a negative sideslip angle and a positive yaw angle when the vanes were extended. As the vanes retracted, free oscillations occurred and the yawing velocities existing were sensed by the yaw damper which produced vertical-tail deflections in a manner to provide damping moments. Time histories of the resulting model motions were obtained by means of the NACA telemetering and instrument system.

The flight conditions of the model are presented in figure 5 where the variations of velocity, dynamic pressure, air density, relative-density factor, and Reynolds number with Mach number are shown. Throughout the flight the level of atmospheric turbulence was low.

ACCURACY AND CORRECTIONS

The estimated probable errors in the basic measured quantities are shown in table III for two Mach numbers (0.8 and 1.4). The lateral derivatives, C_{Y_β}, C_{n_β}, C_{l_β}, C_{l_p}, and $C_{n_r} - C_{n_{\dot{\beta}}}$ are dependent upon some or all of these basic measured quantities. The increments in the various derivatives caused by errors in the basic quantities were determined graphically by the method presented in reference 6, and the results are presented in table IV for $M = 1.4$. The probable errors presented in table IV are given in terms of absolute magnitude as well as percentages of the derivatives, inasmuch as percentage errors have little meaning in some cases. Also shown at the bottom of table IV are the

increments due to a certain amount of uncertainty in the derivatives C_{l_r} and C_{n_p} that had to be estimated in order to determine the other derivatives.

Position corrections to the accelerometer readings were required to correct the measured readings at the instrument location to values at the center of gravity. The angles as measured by the air-flow direction vane mounted in front of the model were corrected for model pitching and yawing velocities to obtain angles of attack and angles of sideslip. Frequency-response corrections to all instruments were not necessary; however, corrections due to instrument lag were applied to the rate of roll and rate of yaw.

RESULTS AND DISCUSSION

Time History

Typical time histories of the free oscillations experienced by the model are shown in figure 6. As stated previously, the yaw-vane disturber was not allowed to operate until the model completely separated from the booster and the motions shown in figure 6 are for the freely flying model after the yaw vanes were retracted. Figure 6(a) presents data after the first deflection of the yaw vanes. It appears from the character of the motions that initially the model experienced cross coupling between the lateral and longitudinal modes of motion and rather large values of angle of sideslip, yawing velocity, and lateral-force coefficient were recorded. A rolling velocity greater than the 3-radian-per-second instrument range was attained and an induced angle of attack was experienced. No attempt was made to analyze this coupled motion. The coupled motion quickly subsided, and during the later part of this oscillation it is felt that the lateral and longitudinal modes were separated. During the time the model experienced coupled motions, the yaw damper system had little effect in damping the induced yawing velocity as shown by the small vertical-tail deflections; however, when the model was oscillating essentially in yaw, the yaw damper quickly damped the motion. No plausible reason can be presented for this erratic operation of the yaw damper except, perhaps, that the rate of roll was so large as to prevent the system from operating satisfactorily due to large inertia and aerodynamic loads. During the remainder of the flight the model was disturbed in yaw and very little induced angle of attack was experienced. (See figs. 6(b), 6(c), and 6(d).)

Throughout the flight the yaw-rate damper system did not function in a consistent manner. This was primarily due to the dead spot in the yaw-rate damper system which became formidable because the model experienced smaller yawing velocities than were expected. Throughout the

flight, during the first portion of each disturbance the δ_t trace had the characteristic of a damped sinusoid. During the latter portion of each disturbance, the δ_t trace either was essentially damped out (when $M > 1.2$) or was oscillating in a random manner (when $M < 1.2$). Thus, no additional damping to the airframe was experienced during the latter portion of each disturbance when the Mach number was greater than 1.2. Therefore, it was possible to analyze the motions of the model while the damper was operative and inoperative. On this basis, then, the characteristics of the lateral oscillations of the airframe-damper combination and the airframe-alone configuration were independently determined when the Mach number was greater than 1.2.

In the remainder of this paper the data are classified according to the operation of the yaw-rate damper; that is, the expressions "damper operative" and "damper inoperative" refer, respectively, to the airframe-damper combination and airframe-alone configuration.

Trim Characteristics

The trim values of the measured quantities are shown in figure 7 for both damper inoperative and damper operative. The data show little difference in the trim characteristics due to the yaw damper system. The positive value of the trim lateral-force coefficient at subsonic and transonic speeds is believed to be a zero shift in the transverse accelerometer. The model experienced a slight transonic trim change in angle of attack, and the mean values of the rolling velocity as given in terms of the wing-tip helix angle $\frac{pb}{2V}$ were less than 0.005 through the Mach number range of the test. It was impossible to obtain trim lift coefficients at supersonic speeds because the model experienced normal accelerations greater than the 5g instrument range.

Oscillation Characteristics

The oscillation characteristics of the model while the damper was operative and inoperative are shown in figures 8 to 13. Values of P and $T_{1/2}$ were determined from all of the measured quantities (β, p, $\dot{\psi}$, C_Y), and the data presented in figures 8 and 9 are the average values obtained.

Figure 8 presents the periods of the lateral oscillations. When damper-operative and damper-inoperative data were available ($M > 1.2$), the yaw-rate damper system had little effect on the periods, which was expected since the design natural frequency of the system was at least six times the natural frequency of the model. An interesting feature

of the data is the relatively constant values of the periods at supersonic speeds.

The damping of the lateral oscillations is shown in figure 9. Although the yaw-rate damper was nonlinear, the data in figure 9 were determined by a linear analysis of the lateral oscillations. Thus, the values of $T_{1/2}$ probably have little significance; however, it is believed that the trend in the data is significant and indicates that the effect of the yaw-rate damper system on the damping of the lateral oscillations is pronounced when the Mach number is greater than 1.2. This effect was also expected since the yaw-rate damper system was designed for $M = 1.6$ and no gain changer was incorporated into the system.

Shown in figure 10 is the critical damping ratio. These data are based on faired curves of the data in figures 8 and 9. Also shown in figure 10 are the design values of the damping ratio for the airframe-damper combination and the airframe-alone configuration. When the Mach number is greater than 1.2, the damping ratio of the airframe-autopilot combination increases whereas that of the airframe-alone configuration decreases with increasing Mach number. Therefore, the effect of the yaw-rate damper system is to add progressively more damping as the Mach number increases. Note that the tendency of the test-data curve is to approach the design data points at $M = 1.6$; however, due to the model experiencing cross coupling (see fig. 6(a)) no data were available to make a direct comparison. The design data point at $M = 1.6$, when the damper is operative, was determined by considering an ideal second-order system for the yaw-rate damper and by estimating a value of the yawing moment due to vertical-tail deflection. The agreement shown in figure 10 might be fortuitous since no effect of a dead spot in the yaw-rate damper system was considered, and a value of the yawing moment due to vertical-tail deflection was estimated.

The phase angle by which the rolling velocity leads the angle of sideslip and the amplitude ratio of rolling velocity to angle of sideslip are shown as a function of Mach number in figure 11. Generally the amplitude ratio increases with increasing Mach number while the phase angle remains relatively constant with increasing Mach number. The yaw-rate damper system had little effect on the amplitude ratio and phase when the Mach number was greater than 1.2.

Figure 12 represents the variation of the phase angle by which the yawing velocity leads the angle of sideslip and the amplitude ratio of yawing velocity to angle of sideslip as a function of Mach number. When the Mach number was greater than 1.2, the yaw-rate damper system had little effect on the amplitude ratio $\left|\frac{\dot{\psi}}{\beta}\right|$; however, the effect of the

yaw-rate damper system was to increase the phase angle between the yawing velocity and angle of sideslip. This increase in the phase angle was primarily due to the addition of an aerodynamic yawing moment due to vertical-tail deflection in the yawing-moment equation which changed the modal characteristics and resulted in an increase in the effective damping in yaw. No attempt was made to fair the data that appear in figures 11 and 12 since each point constitutes a faired value for a number of half-cycles of oscillations.

Presented in figure 13 is the variation of the gain and phase of the yaw-rate damper system with Mach number. Shown are the flight-test values, design values, and the effect of the dead spot in the system for two values of yaw-rate input. The two values were chosen to show the effect of the nonlinearity of the damper system on the output. The value of $\dot{\psi} = 1.0$ radian/second corresponds to the value which was used in the design of the yaw-rate damper system, whereas the value of $\dot{\psi} = 0.2$ radian/second corresponds to the order of the measured values as obtained from the flight test. A discussion of the dead spot as well as the phase lag due to the dead spot and the system dynamics is presented in the appendix. As the amplitude of the yaw-rate input is decreased, the effect of the dead spot is seen to decrease the gain and increase the phase lag between the δ_t output and $\dot{\psi}$ input. It can be shown that, as the output approaches the dead spot, the phase lag approaches 90°. Thus, the effect of the dead spot becomes formidable as the yaw-rate input approaches the values measured from the flight test. No direct comparison can be made between the measured flight-test values and the computed values considering the dead spot since the amplitude of the yaw-rate input varied with Mach number. It is believed that the values of the gain were more accurately determined from the flight-test data then were the phase lags, particularly at subsonic speeds, since the yaw-rate input approached the accuracy of the gyro-type instrument that was used to measure the yaw-rate input.

Flying Qualities

The oscillatory characteristics presented previously for both the airframe-damper combination and airframe-alone configuration may be interpreted in terms of full-scale-airplane flying qualities. The non-dimensional characteristics of the motion may be considered as applying to the full-scale airplane having the same relative density and non-dimensional radii of gyration.

The relative-density factor for the present test was presented in figure 5. Full-scale altitudes and wing loadings for $M = 1.4$ based on the relative-density factor at this Mach number and assuming the model was a 1/10-scale model are shown in figure 14. These values obtained with the model are representative of current aircraft.

The requirements for damping of the lateral oscillations as stated in reference 8 are shown in figure 15. Shown in the figure are points at $M = 1.4$ for both the damper operative and inoperative portions of the flight test. The data indicate that the damping is marginal for the airframe alone and is satisfactory during tactical missions for the airframe-damper combination.

A comparison was made of the radii of gyration of the model with average values for three current swept-wing fighter airplanes in order to determine whether the data in figure 15 were applicable to a full-scale airplane. The comparison showed that the nondimensional radii of gyration in roll were about the same, but the nondimensional radius of gyration in yaw of the model was about 30 percent higher than those of current swept-wing airplanes. Thus, it appears that the model does not simulate a full-scale airplane. The effect of a 30-percent decrease in the radius of gyration in yaw is to move the data points in figure 15 farther into the satisfactory range and thereby to make the full-scale-airplane lateral damping characteristics better than those shown in the figure.

An additional lateral oscillatory requirement stated in reference 8 is that the ratio of roll angle to angle of sideslip $\left|\frac{\phi}{\beta}\right|$ should not exceed 4 in order to prevent large rolling motions due to small changes in heading or rough air. Presented in figure 16 is the variation of $\left|\frac{\phi}{\beta}\right|$ with Mach number for both the damper-inoperative and damper-operative portions of the flight test. The data indicate that the effect of the yaw damper system is negligible and that at subsonic speeds $\left|\frac{\phi}{\beta}\right|$ exceeded 4, whereas at supersonic speeds $\left|\frac{\phi}{\beta}\right|$ was about 4. The effect of a 30-percent decrease in the radius of gyration in yaw would be to decrease the values of $\left|\frac{\phi}{\beta}\right|$ shown.

Lateral-Stability Derivatives

Lateral-force derivative.- Typical plots of the variation of lateral-force coefficient with angle of sideslip are shown in figure 17 where, within the random scatter of the data, the curves appear to be linear. The data in figure 17 are for the damper-operative portion of the flight test. Plots of the variation of lateral-force coefficient with angle of sideslip were also determined for the damper-inoperative portion of the flight test and although not presented are similar to those shown in figure 17.

From the plots of lateral-force coefficients against angle of sideslip, the slopes were determined and the variation of lateral-force derivative C_{Y_β} with Mach number are shown in figure 18 for both damper inoperative and operative portions of the flight test. The data show the usual variation of C_{Y_β} with Mach number for configurations having sweptback surfaces, and the effect of the auxiliary yaw-rate damper system on C_{Y_β} was negligible. The estimated rigid values were determined by the method presented in appendix B of reference 7 and indicate that the vertical-tail flexibility had a relatively small effect on C_{Y_β}.

Vector plots.- The oscillatory characteristics when the yaw damper system was inoperative were analyzed by the time-vector method to determine the lateral stability derivatives C_{n_β}, C_{l_β}, C_{l_p}, and $C_{n_r} - C_{n_{\dot\beta}}$ of the airframe-alone configuration. The techniques and procedure involved in analyzing oscillatory motions by the time-vector method are well known at this time and detailed explanations have been presented, for example, in references 5 to 7 and references 9 and 10. No details of the method are presented in this paper since they are fully covered in the above-mentioned references. However, for completeness a typical time-vector solution of the lateral equations of motion is presented in figure 19. The solution of the lateral-force equation appears in figure 19(a), the solution of the rolling-moment equation appears in figure 19(b), and the solution of the yawing-moment equation appears in figure 19(c). These solutions are presented for $M = 1.40$.

The lateral-stability derivatives obtained when the yaw damper system was inoperative - that is, during the latter part of the disturbances when the Mach number was greater that 1.2 - are listed in the following table:

	M	
	1.40	1.27
C_{n_β}	0.150	0.192
C_{l_β}	-0.055	-0.060
C_{l_p}	-0.345	-0.373
$C_{n_r} - C_{n_{\dot\beta}}$	0	-0.520

Values of C_{n_β} and $C_{n_r} - C_{n_{\dot{\beta}}}$ were determined by the vector method for an estimated value of $C_{n_p} = 0.05$; whereas, the values of C_{l_β} and C_{l_p} were determined by the vector method for an estimated value of $C_{l_r} = 0.10$. The possible effects of inertia coupling have been investigated and the effects on the dynamic lateral stability derivatives that appear in the table were found to be small.

CONCLUSIONS

A lateral stability investigation was conducted to provide some additional experience with model testing of automatic controls and to provide further information on the effect of an auxiliary yaw damper sensitive to yawing angular velocity on the lateral stability of high-performance airplanes. From the results of this investigation utilizing a rocket-propelled model of a 45° sweptback-airplane configuration equipped with an auxiliary yaw-rate damper designed for supersonic speeds with no gain-changer provisions the following conclusions are indicated:

1. The yaw-rate damper system was nonlinear due to a relatively large dead spot in the system.

2. The effect of the yaw-rate damper system, where data were available ($M > 1.2$), was to increase the damping of the lateral oscillations.

3. When the results are interpreted in terms of full-scale-airplane flying qualities, the yaw-rate damper system had a large effect on the lateral damping at a Mach number of 1.4.

Langley Aeronautical Laboratory,
National Advisory Committee for Aeronautics,
Langley Field, Va., November 29, 1956.

APPENDIX

YAW-RATE DAMPER SYSTEM

Description

The yaw-rate damper system consists of a rate gyro connected mechanically to the valve of a pneumatic servo. (See fig. 20 and sketch 1.)

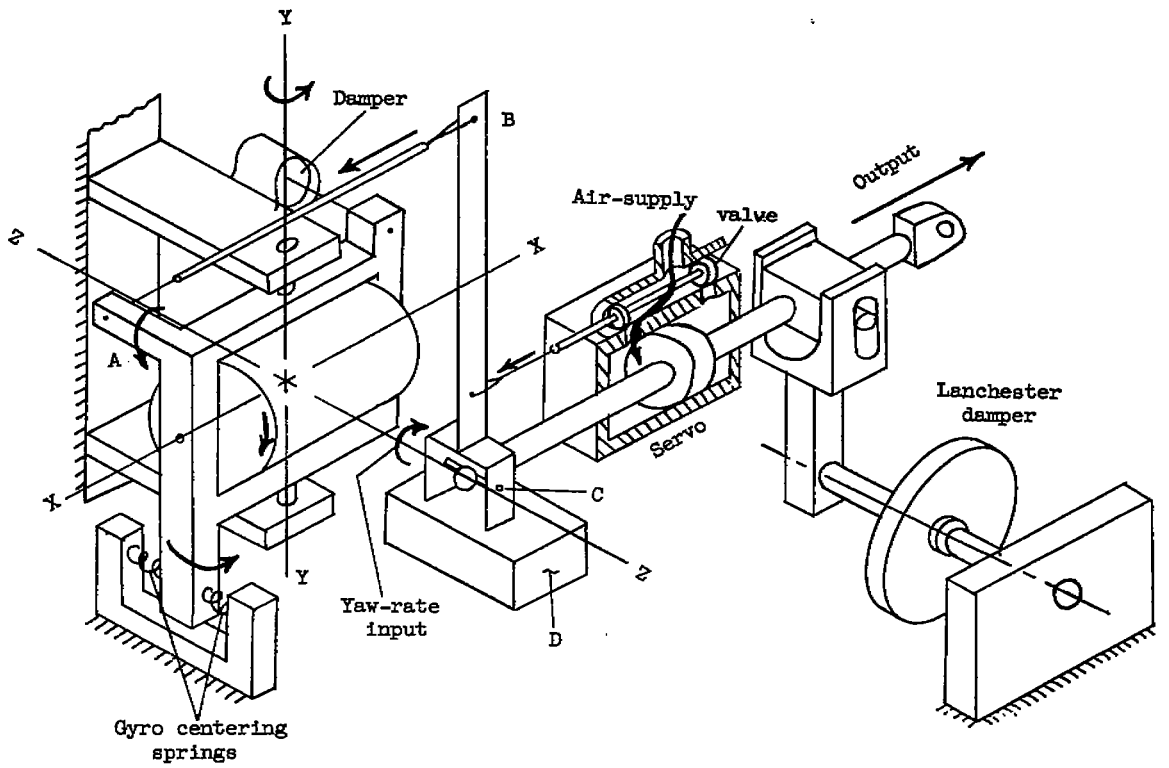

Sketch 1

In the diagram it can be seen that the linkage is by means of a floating member or whiffletree (B) which has a mass (D) at one end. In operation, when the gyro output arm (A) moves, it displaces the valve by pivoting the whiffletree about point (C). The valve now causes the servo to move until the valve is in its original position. This movement may be very rapid, which causes a restoring force to the gyro arm (A) due to the tendency of the mass (D) to remain stationary. The restoring force is proportional to the acceleration of the servo. This feedback is necessary to stabilize the system.

Tests

The yaw damper was designed for flight conditions at $M = 1.6$ and no gain-changes provisions were incorporated. The design gain was $\left|\frac{\delta}{\dot{\psi}}\right| = 0.07$ deg/deg/sec, and it was desired that the natural frequency be as much in excess of 100 radians/second as possible. It was anticipated that the system would be critically damped under these conditions. The following bench tests were performed in order to check the design specifications:

1. The system was placed on a rotating table and the rate-gyro speed and the gyro centering springs were adjusted to meet the design gain. While on the rotating table the dead spot in the system due to valve overlap was measured to be 0.45° of control-surface deflection.

2. The dynamic stability of the system was first checked with the simulated aerodynamic hinge moment equal to zero. This was done by moving the gyro gimbal to full deflection and then releasing it while the system was loaded with the designed inertia load. The resulting transient is shown in sketch 2(a).

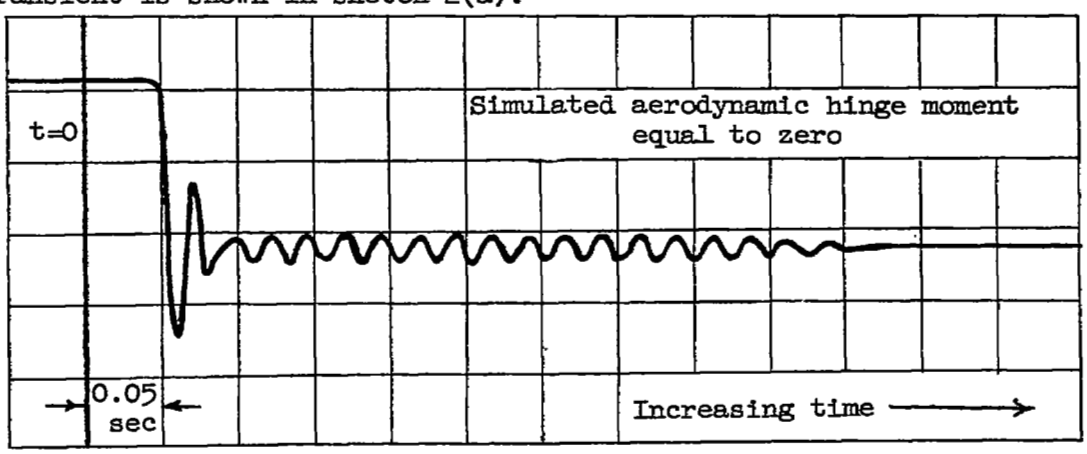

Sketch 2a

3. The same dynamic stability test was performed with the design aerodynamic hinge moment simulated by springs. This transient is shown in sketch 2(b).

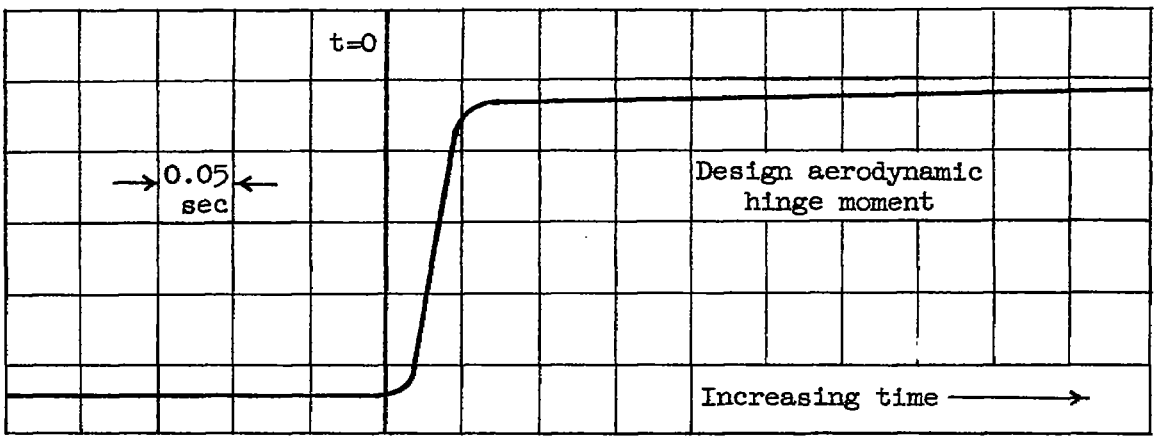

Sketch 2b

4. No attempt was made to measure the frequency response of the system.

The natural frequency of the system was obtained from the zero-aerodynamic-hinge-moment transient (sketch 2(a)) and was determined to be 129.5 radians/sec. This value was taken to be the undamped natural frequency of the system. The damping was determined from the design-aerodynamic-hinge-moment transient (sketch 2(b)) by comparing the time to reach 95 percent of full servo throw with a family of transient curves (see ref. 11) and was found to be about 1.0.

In estimating the damping, it was assumed that there was no appreciable change in the undamped natural frequency between the conditions of zero aerodynamic hinge moment and design aerodynamic hinge moment because of the following reasons:

1. In bench tests, the undamped natural frequency was observed to vary with the stiffness of the gyro centering springs. For example, a trial spring gave an undamped natural frequency of over 300 radians/sec.

2. Further, no sensible change occurred in the design undamped natural frequency of 129.5 radians/sec when the inertia load was varied 400 percent while operating under zero aerodynamic hinge moment. For this purpose the inertia loads were considered equivalent to the aerodynamic loads.

The conclusion was thus drawn that the gyro centering springs were the controlling factor in determining the natural frequency of the system.

The difference in damping exhibited in sketch 2 is believed largely due to the fact that, as this is an air system and air is compressible, the flow through the valve varies greatly between the zero-aerodynamic-hinge-moment and design-aerodynamic-hinge-moment conditions. Apparently the increase in damping comes from these altered flow characteristics. There is also the Bernoulli effect which causes a strong centering force on the valve. This varies with valve opening and it would be difficult to estimate its part in these phenomena.

Effect of Dead Spot

The finished airframe was built with a rudder linkage which gave a throw of $\pm 10^{\circ}$ rather than $\pm 5^{\circ}$ for full servo stroke as was originally specified. This resulted in using only one-half the servo stroke at the designed gain. Due to space limitations it was only possible to modify this to $\pm 7.2^{\circ}$.

When the model was flown, the yawing velocity produced by the pulse yaw vanes was less then expected. Consequently, the maximum deflection of the vertical tail was less then 1°. This plus the linkage change described above meant that approximately 1/9 of the servo travel was the maximum amount ever used. In estimating the phase lag due to the valve action, the following assumptions were made, which offer a possible explanation of the dead spot based on static conditions. However with high rates, these results would be overshadowed.

1. The dead spot was entirely in the valve; it was sharp and no dynamics were involved.

2. The dead spot assumed was the maximum the system could develop and probably no greater than that which actually existed.

3. It was further assumed from the $\dot{\psi}$ step input that the damping ratio was 1.0. Inspection of the transient response shown in sketch 2 shows that the curves are not those of a linear system; however, the assumption $\zeta = 1.0$ is probably as close an approximation as can be made.

Readings of amplitude ratio $\left|\frac{\delta}{\dot{\psi}}\right|$ and phase angle $\Phi_{\delta\dot{\psi}}$ from the flight-test records showed that both the gain and the phase of the yaw-damper-system output were not as expected.

In order to evaluate better the results, a graphical analysis was made for two yaw-rate inputs at $M = 1.6$ as shown in sketch 3.

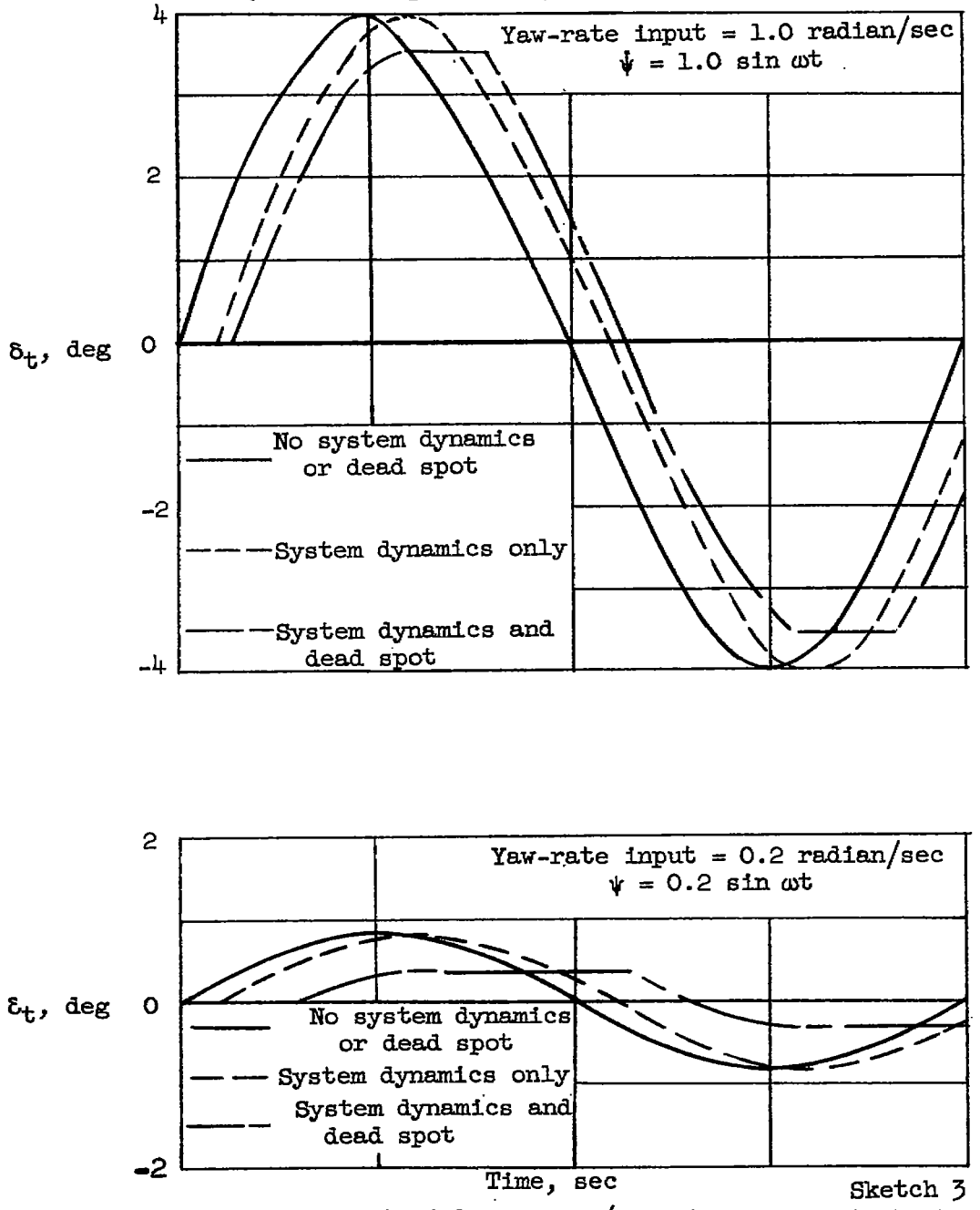

Sketch 3

The yaw-rate input of 1.0 radian/second corresponds to the value which was used in the design of the yaw-rate damper system, whereas the

yaw-rate input of 0.2 radian/second corresponds to the order of the measured values at subsonic speeds. Shown in sketch 3 is the output δ_t determined by first considering no system dynamics or dead spot (ideal damper), then by considering system dynamics alone, and finally by considering system dynamics and dead spot together.

The phase lag due to the system dynamics is a function of its damping ratio and the airframe and damper natural frequencies. The natural frequency of the model is shown in figure 21; the phase lag as a function of the damping ratio ζ, model undamped natural frequency ω_n, and the damper natural frequency ω is shown in figure 22. The phase lags were determined from the expression shown in the figure, which was taken from reference 12, and ζ was assumed to be equal to 1.0.

The phase lag due to the dead spot in the system is a function of the known dead spot and the magnitude of δ_t as shown by the expression

$$\Phi_{\delta\dot{\psi}} = \frac{0.45}{\delta_t + 0.45}$$

As may be seen in sketch 3, the effect of the dead spot in the system on the output δ_t becomes greater as the yaw-rate input becomes smaller. When the yaw-rate input was equal to 1.0 radian/second, the phase lag due to system dynamics alone was about 18°, whereas the phase lag due to system dynamics and dead spot was about 24°. However, when the yaw-rate input was 0.2 radian/second, the respective phase lags were 18° and 54°.

Thus, for the flight conditions experienced by the model, the effect of the dead spot in the yaw-rate damper system was formidable and resulted in values of the phase angle $\Phi_{\delta\dot{\psi}}$ that were considerably larger than were expected. Consequently, the damping contributed by the system was less than was expected.

REFERENCES

1. Gates, Ordway B., Jr.: A Theoretical Analysis of the Effects of Several Auxiliary Damping Devices on the Lateral Stability and Controllability of a High-Speed Aircraft. NACA TN 2565, 1951.

2. Gates, Ordway B., Jr., and Sternfield, Leonard: Effect of an Autopilot Sensitive to Yawing Velocity on the Lateral Stability of a Typical High-Speed Airplane. NACA TN 2470, 1951.

3. White, Roland J.: Investigation of Lateral Dynamic Stability in the XB-47 Airplane. Jour. Aero. Sci., vol. 17, no. 3, Mar. 1950, pp. 133-148.

4. Moul, Martin T.: Flight Investigation of a Supersonic Canard Missile Equipped With an Auxiliary Damping-in-Pitch Control System. NACA RM L52K14b, 1953.

5. D'Aiutolo, Charles T., and Henning, Allen B.: Lateral Stability Characteristics at Low Lift Between Mach Numbers of 0.85 and 1.15 of a Rocket-Propelled Model of a Supersonic Airplane Configuration Having a Tapered Wing With Circular-Arc Sections and 40° Sweepback. NACA RM L55A31, 1955.

6. Mitchell, Jesse L., and Peck, Robert F.: Investigation of the Lateral Stability Characteristics of the Douglas X-3 Configuration at Mach Numbers From 0.6 to 1.1 by Means of a Rocket-Propelled Model. NACA RM L54L20, 1955.

7. Gillis, Clarence L., and Chapman, Rowe, Jr.: Effect of Wing Height and Dihedral on the Lateral Stability Characteristics at Low Lift of a 45° Swept-Wing Airplane Configuration As Obtained From Time-Vector Analyses of Rocket-Propelled-Model Flights at Mach Numbers From 0.7 to 1.3. NACA RM L56E17, 1956.

8. Flying Qualities of Piloted Airplanes. Military Specification, MIL-F-8785 (ASG), Sept. 1, 1954.

9. Wolowicz, Chester H.: Time-Vector Determined Lateral Derivatives of a Swept-Wing Fighter-Type Airplane With Three Different Vertical Tails at Mach Numbers Between 0.70 and 1.48. NACA RM H56C20, 1956.

10. Breuhaus, W. O.: Resumé of the Time Vector Method as a Means for Analyzing Aircraft Stability Problems. WADC Tech, Rep. 52-299 (Contract No. AF33(038)-20659 RDO No. 461-1-2), Wright Air Dev. Center, U.S. Air Force, Nov. 1952.

11. Nixon, Floyd E.: Principles of Automatic Controls. Prentice-Hall, Inc., c. 1953, p. 27.

12. Chestnut, Harold, and Mayer, Robert W.: Servomechanisms and Regulating System Design. Vol. I. John Wiley & Sons, Inc., 1951, p. 312.

TABLE I

GEOMETRIC CHARACTERISTICS

Wing:

Total area, sq ft	5.76
Span, ft	4.80
Aspect ratio	4.0
Mean aerodynamic chord, ft	1.32
Sweep of quarter-chord line, deg	45
Taper ratio	0.3
Airfoil section	65A006

Horizontal tail:

Total area, sq ft	0.835
Span, ft	1.83
Aspect ratio	4.0
Mean aerodynamic chord, ft	0.50
Sweep of quarter-chord line, deg	45
Taper ratio	0.30
Airfoil section	65A006

Vertical tail:

	Total	Exposed
Area, sq ft	0.88	0.585
Span, ft	1.18	0.917
Aspect ratio	1.59	1.43
Mean aerodynamic chord, ft	0.82	0.685
Sweep of quarter-chord line, deg	45	45
Taper ratio	0.30	0.368
Airfoil section	65A006	65A006

Fuselage:

Length, ft	8.25
Fineness ratio	12.25

TABLE II

MASS AND INERTIA CHARACTERISTICS

Weight, lb	166.5
Center-of-gravity position, percent $\bar{c}$	25
Moments of inertia, slug-ft^2:	
Pitch	25.38
Yaw	26.88
Roll	1.50
Inclination of principal axis, deg	0.5
Radii of gyration, ft:	
Pitch	2.22
Yaw	2.28
Roll	0.54
Natural frequencies, cps:	
Wing first bending	58
Wing second bending	202
Horizontal-tail first bending	108
Horizontal-tail second bending	348

TABLE III

ESTIMATED ACCURACY OF VARIOUS MEASURED QUANTITIES

[All increments may be positive or negative]

Quantity	Accuracy	
	M = 1.4	M = 0.8
W	0.5 percent	0.5 percent
I_X	3.0 percent	3.0 percent
I_Z	1.0 percent	1.0 percent
ϵ	0.5°	0.5°
α,β	0.5°	0.5°
M	1.0 percent	2.0 percent
q	2.0 percent	6.0 percent
a	0.05 sec	0.10 sec
P	0.005 sec	0.010 sec
$\left\lvert\frac{p}{\beta}\right\rvert$	3.0 percent	3.0 percent
$\Phi_{p\beta}$	3.0°	3.0°
$\left\lvert\frac{A_T/g}{\beta}\right\rvert$	2.0 percent	2.0 percent

TABLE IV

CALCULATED ACCURACY OF AERODYNAMIC DERIVATIVES FOR M = 1.4

[All increments may be positive or negative, and all derivatives are for β in radians]

Increment due to error in -	ΔC_{Y_β}	ΔC_{n_β}	ΔC_{l_β}	ΔC_{l_p}	$\Delta\left(C_{n_r} - C_{n_{\dot{\beta}}}\right)$
W	0.003	0.001	0.001	0.005	0.01
I_Z	-----	.002	-----	-----	.02
I_X	-----	-----	.003	.014	----
ϵ	-----	.003	.001	.001	.03
α	-----	.003	0	0	.01
$\left\lvert \frac{A_T/g}{\beta} \right\rvert$	.013	0	0	0	0
q	.014	.003	.001	.005	.02
a	-----	0	0	0	.03
P	-----	.003	.002	.003	.01
$\left\lvert \frac{p}{\beta} \right\rvert$	-----	.001	.004	.007	.02
$\Phi_{p\beta}$	-----	.001	.003	.045	.02
Probable error $\sqrt{\Sigma(\Delta)^2}$	.020	.007	.006	.048	.06
Value of derivative	-.595	.145	-.068	-.445	.00
Probable error percent derivative	3	5	9	11	∞

Increment due to -	ΔC_{Y_β}	ΔC_{n_β}	ΔC_{l_β}	ΔC_{l_p}	$\Delta\left(C_{n_r} - C_{n_{\dot{\beta}}}\right)$
0.1 change in C_{l_r}	-----	-----	0.004	0.003	----
0.1 change in C_{n_p}	-----	.010	-----	-----	.190

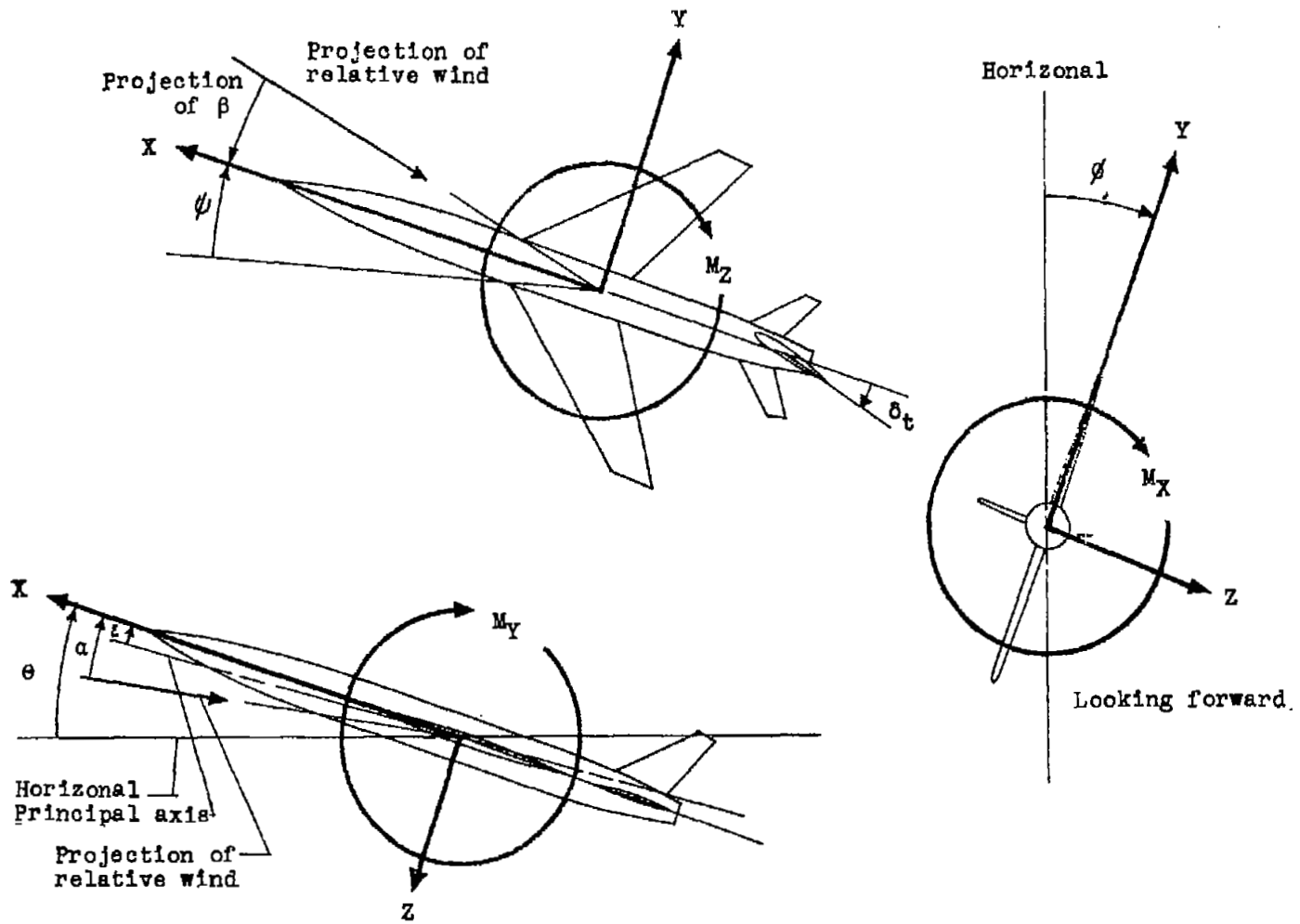

Figure 1.- Sketch showing the body axes system. Each view presents a plane of the axis system as viewed along the third axis. Arrows indicate positive directions of forces, moments, and angles.

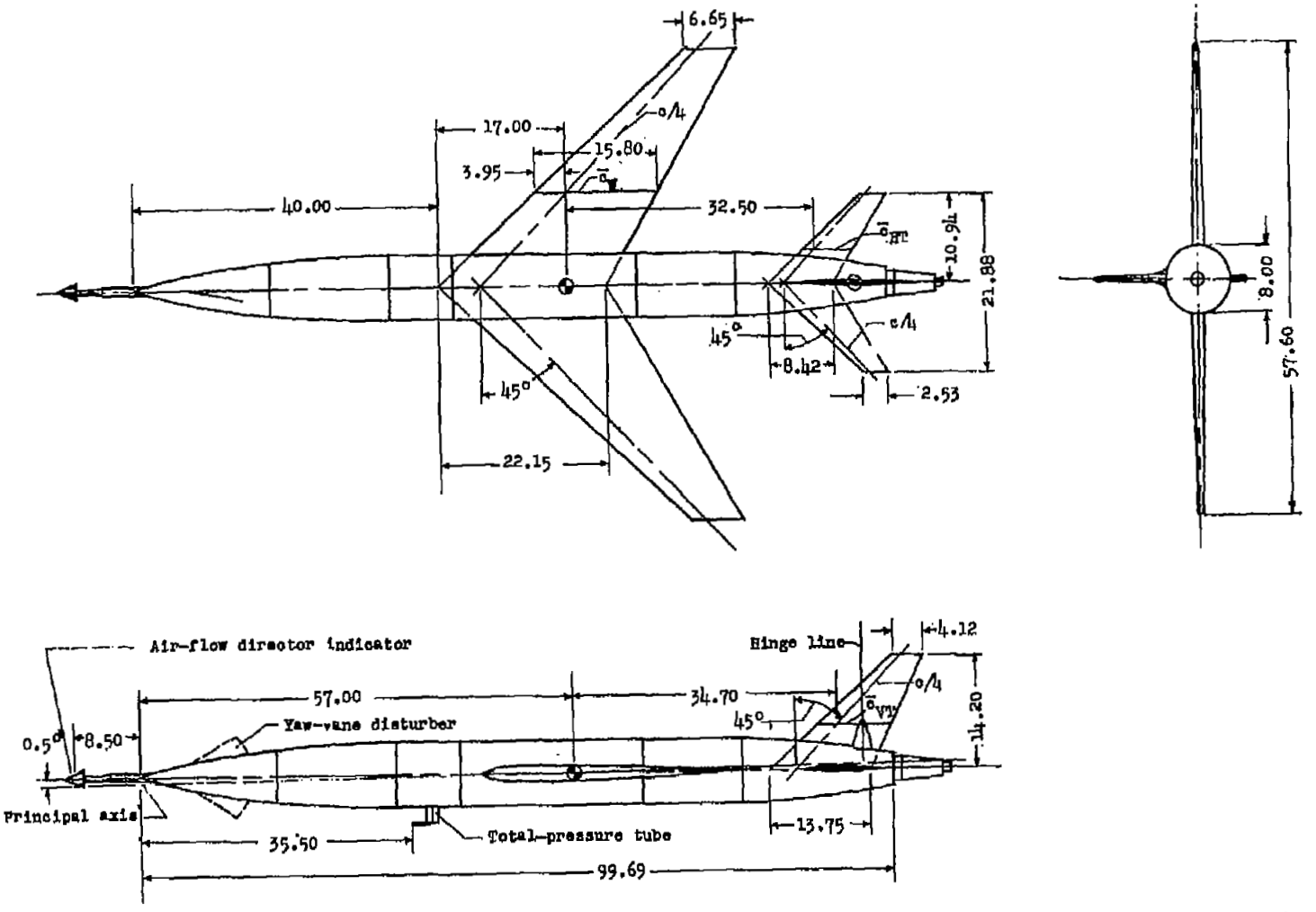

Figure 2.- General arrangement of model. All dimensions are in inches unless otherwise noted.

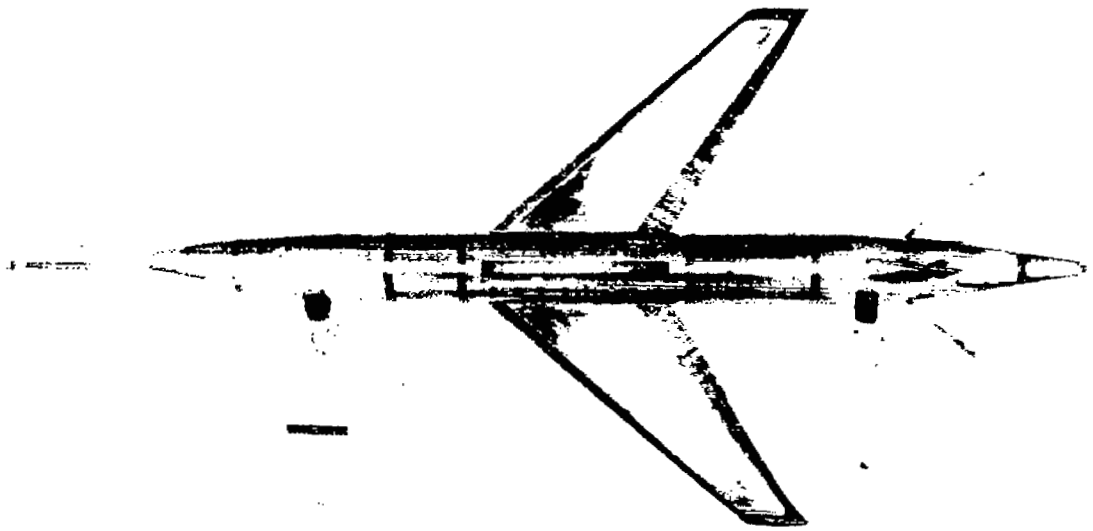

(a) Top view of model. L-91100.1

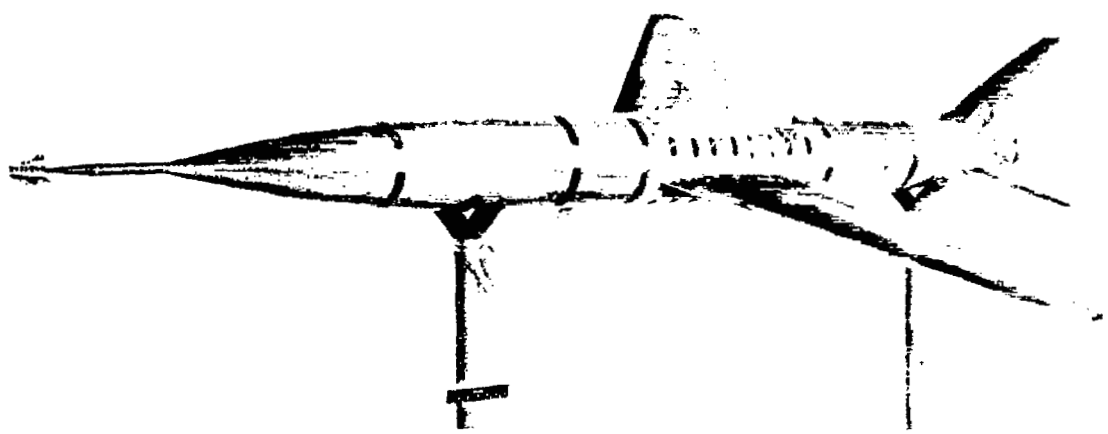

(b) Three-quarter front view of model. L-91097.1

Figure 3.- Model and model-booster combination.

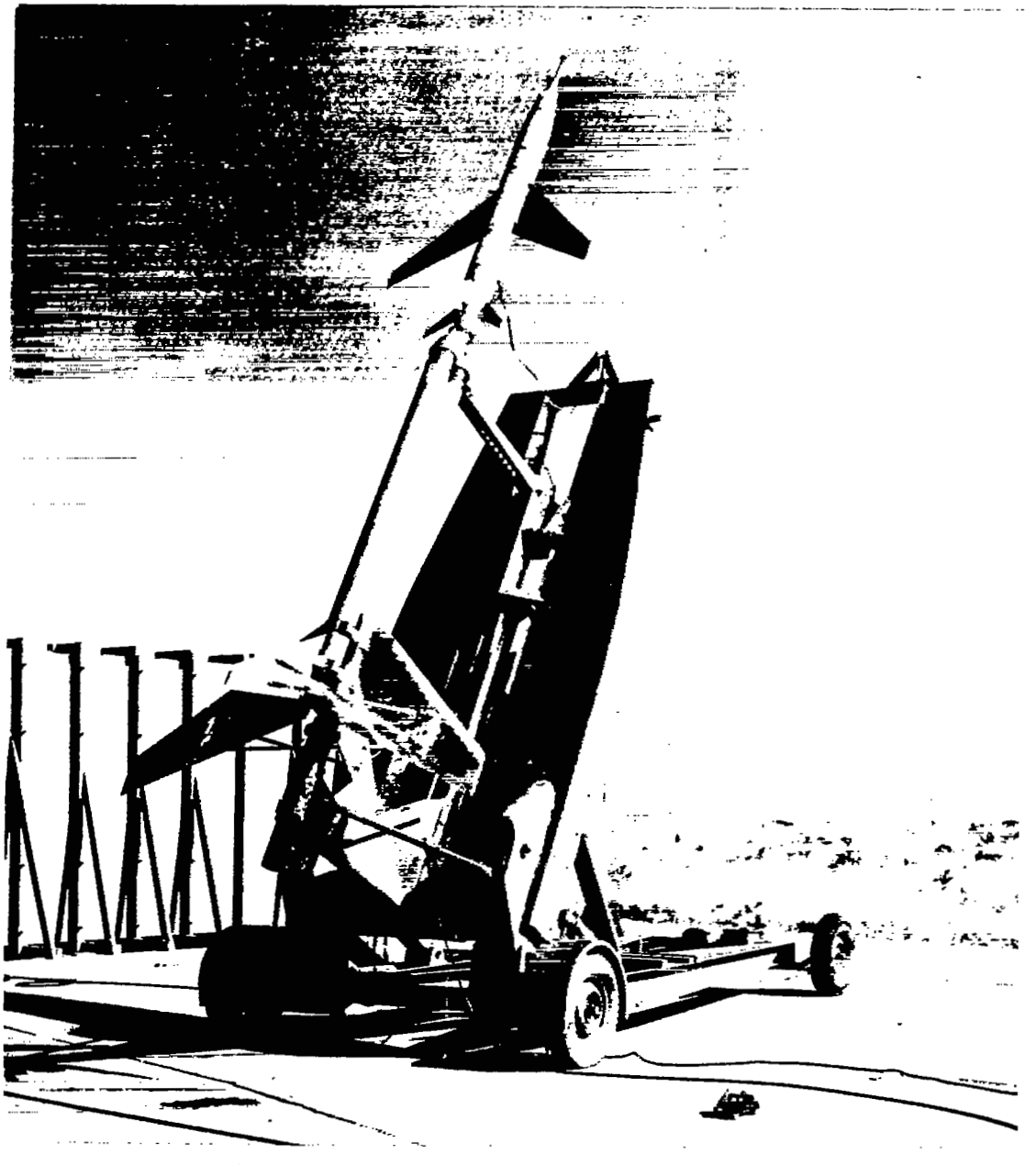

(c) Model-booster combination on launcher. L-91325

Figure 3.- Concluded.

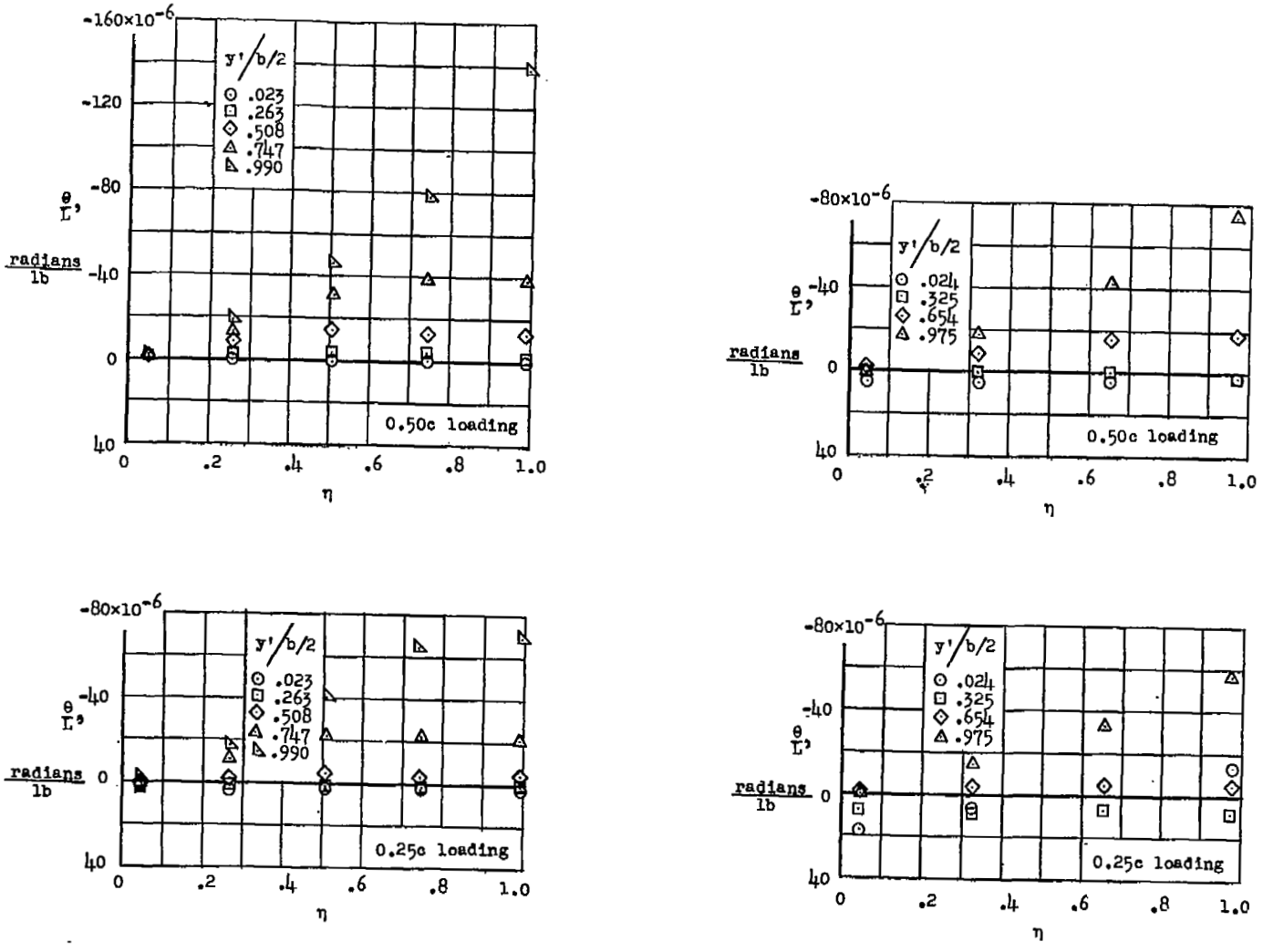

(a) Wing.

(b) Vertical tail.

Figure 4.- Measured influence coefficients.

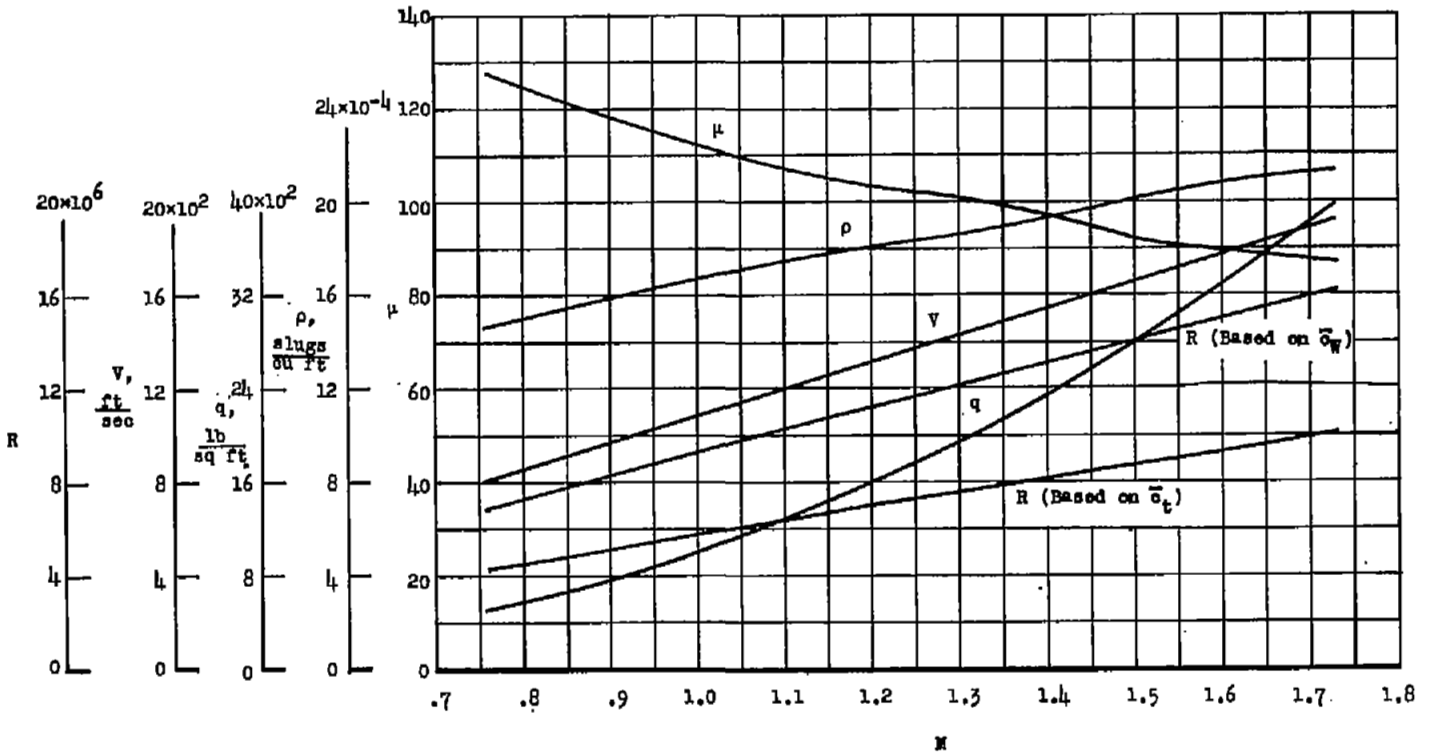

Figure 5.- Variation of velocity, dynamic pressure, air density, relative-density factor and Reynolds number with Mach number.

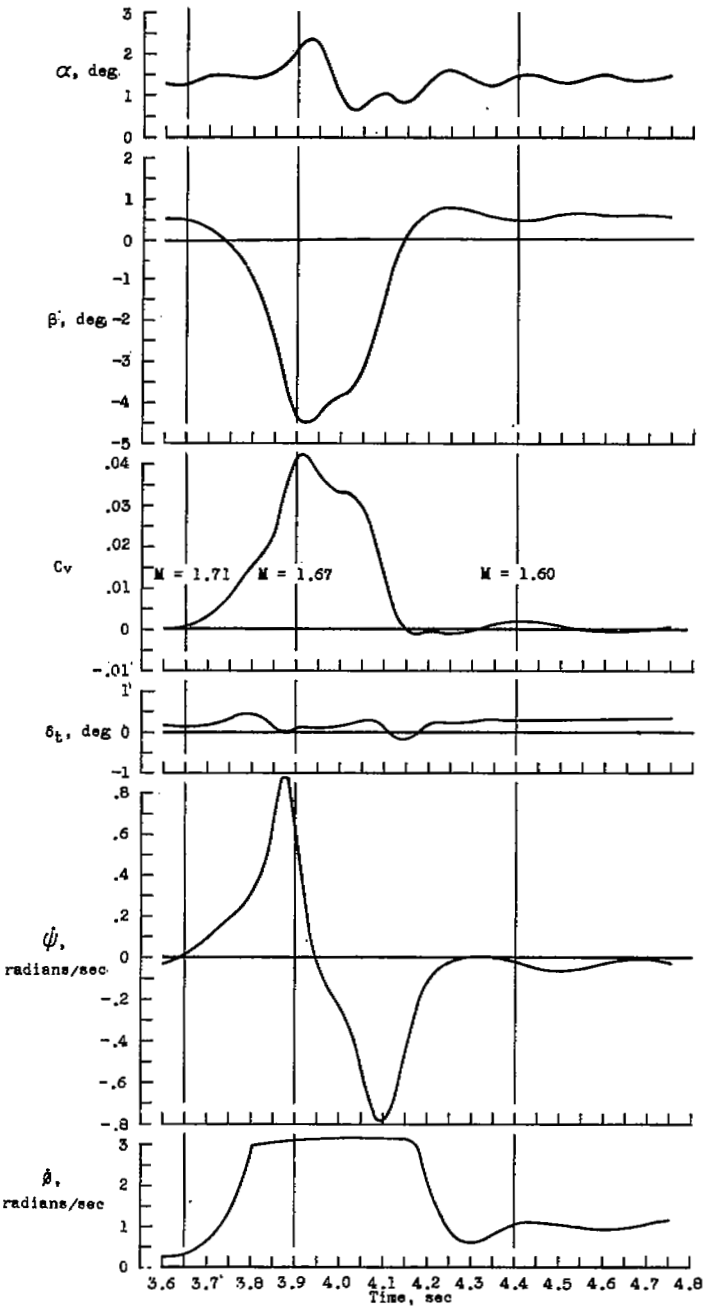

(a) $1.71 \leqq M \geqq 1.55$.

Figure 6.- Typical time histories.

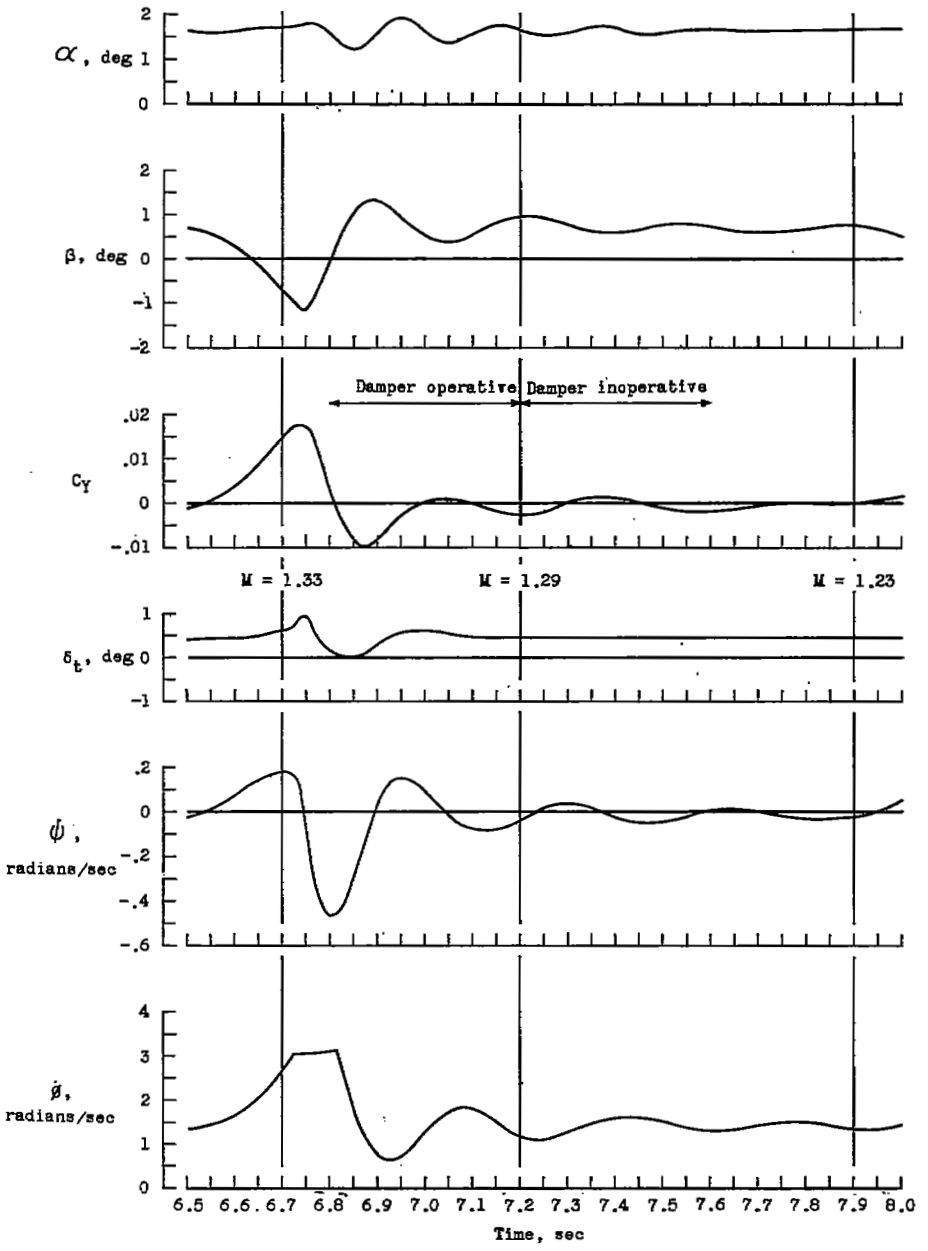

(b) $1.35 \leqq M \geqq 1.22$.

Figure 6.- Continued.

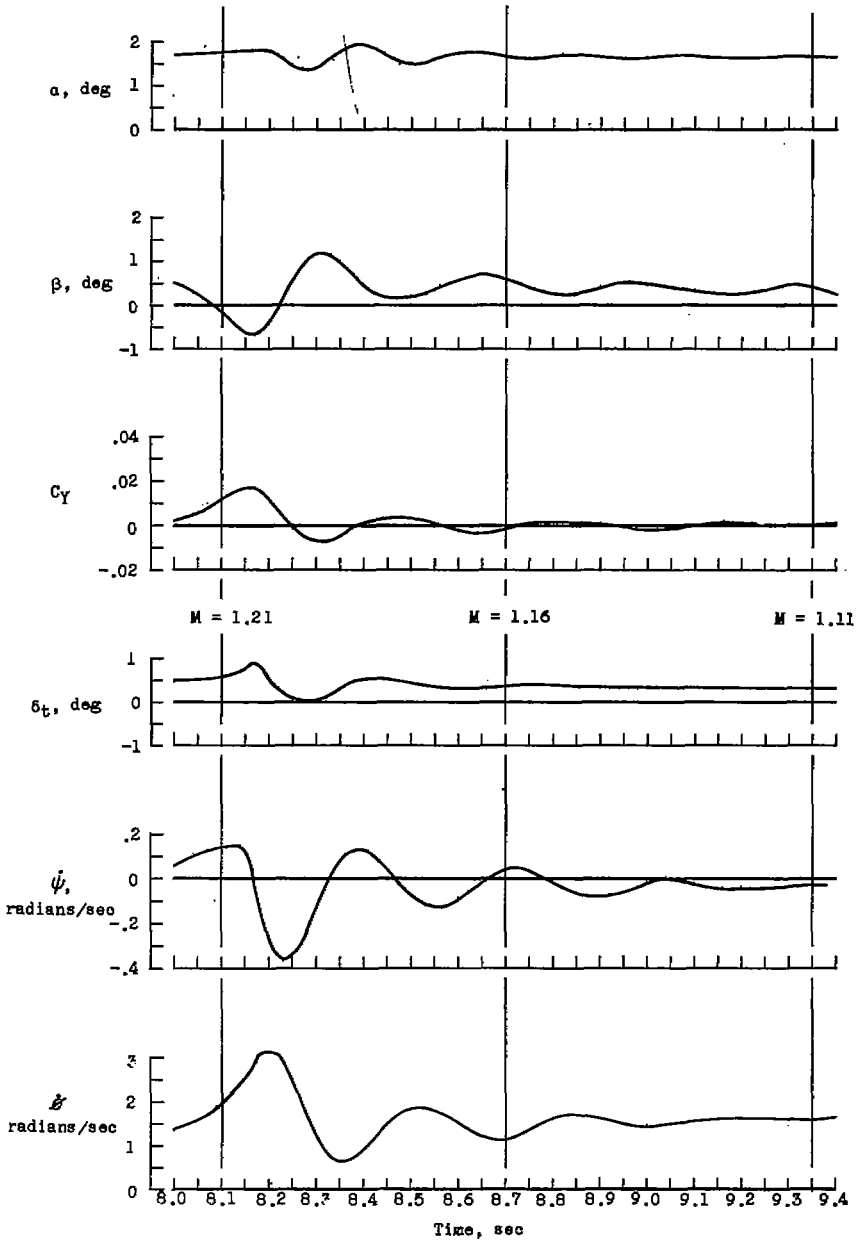

(c) $1.22 \leqq M \geqq 1.11$.

Figure 6.- Continued.

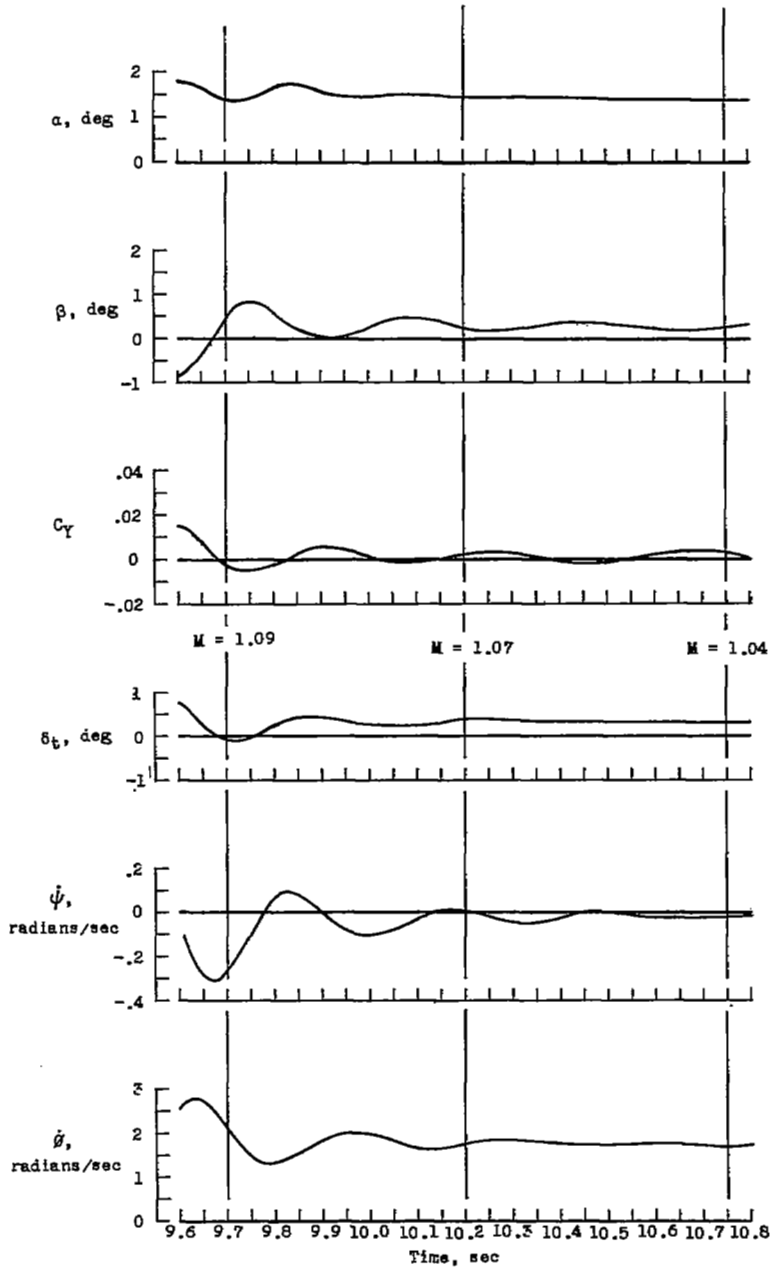

(d) $1.10 \leqq M \geqq 1.04$.

Figure 6.- Continued.

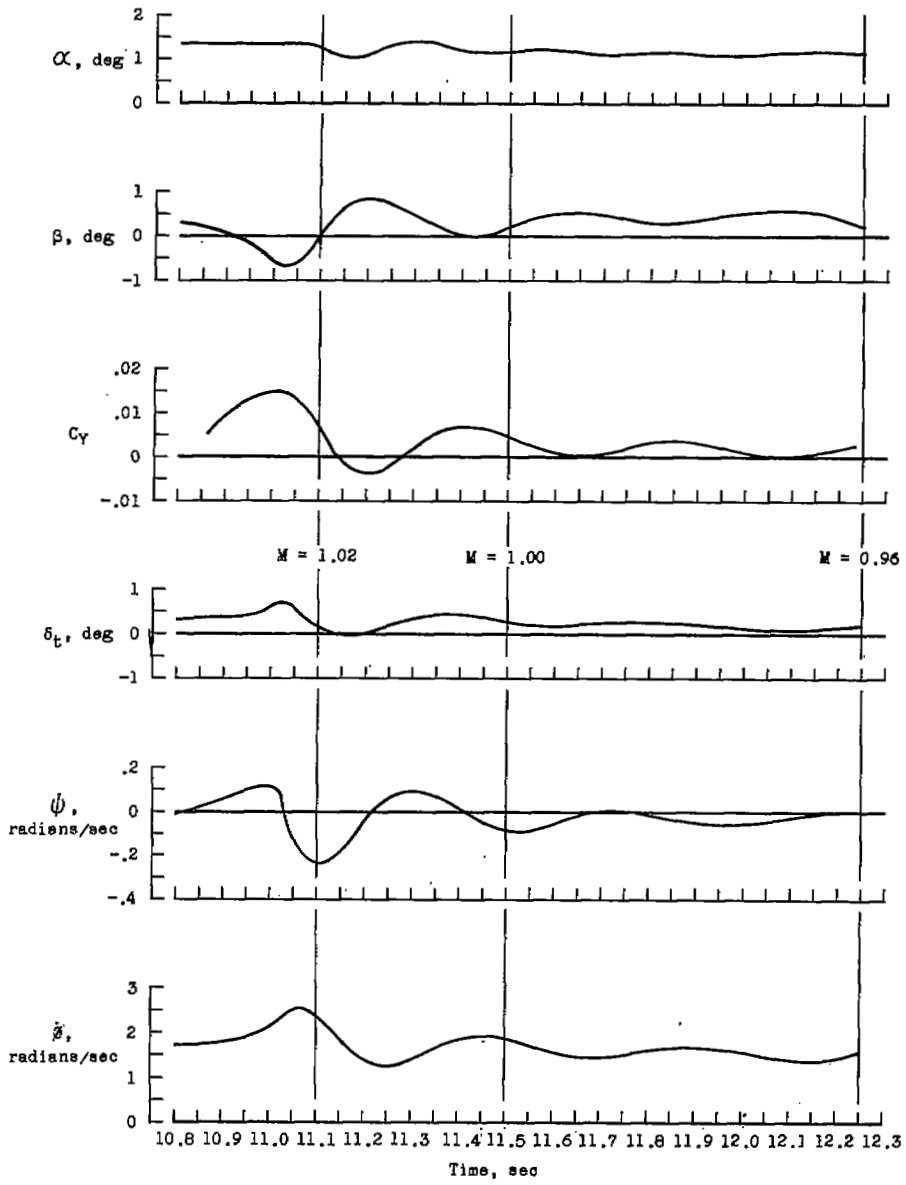

(e) $1.04 \leqq M \geqq 0.96$.

Figure 6.- Continued.

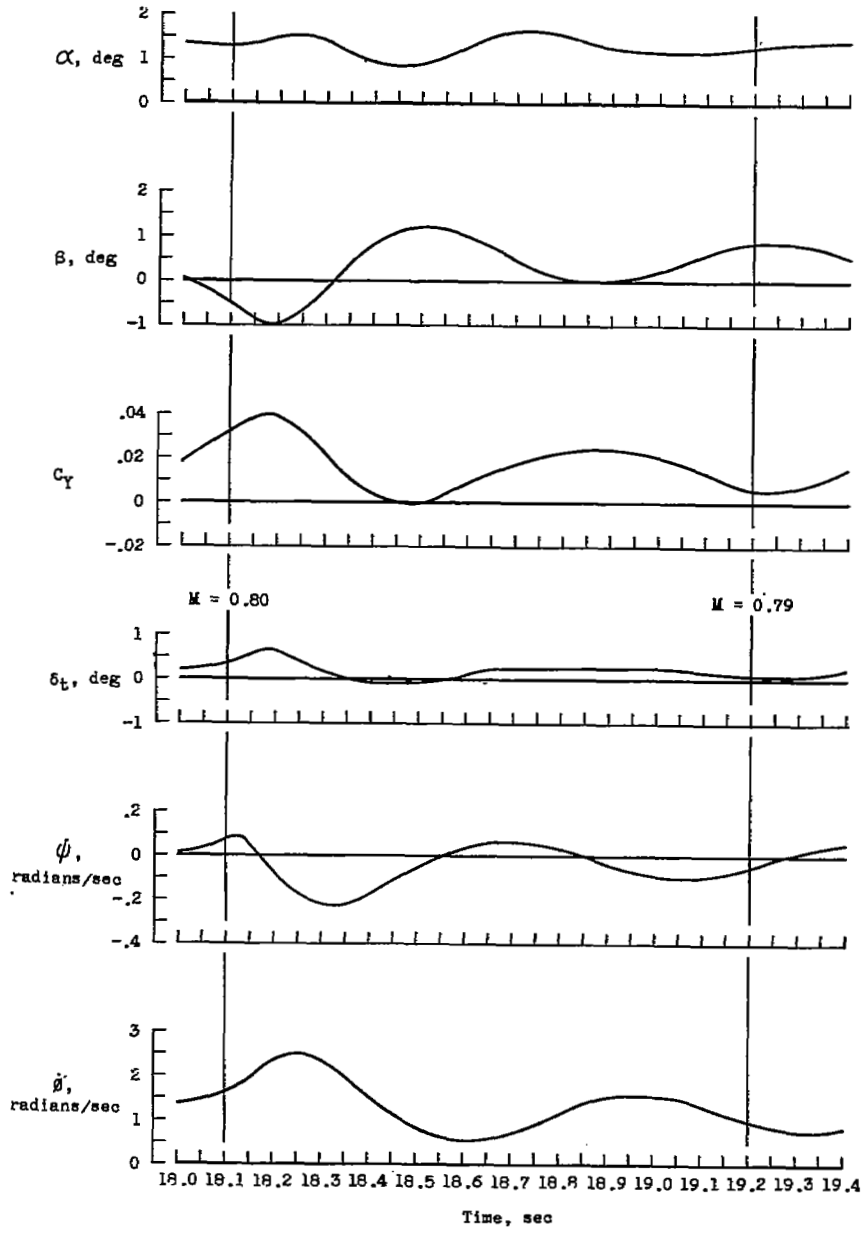

(f) $0.80 \leqq M \geqq 0.79$.

Figure 6.- Concluded.

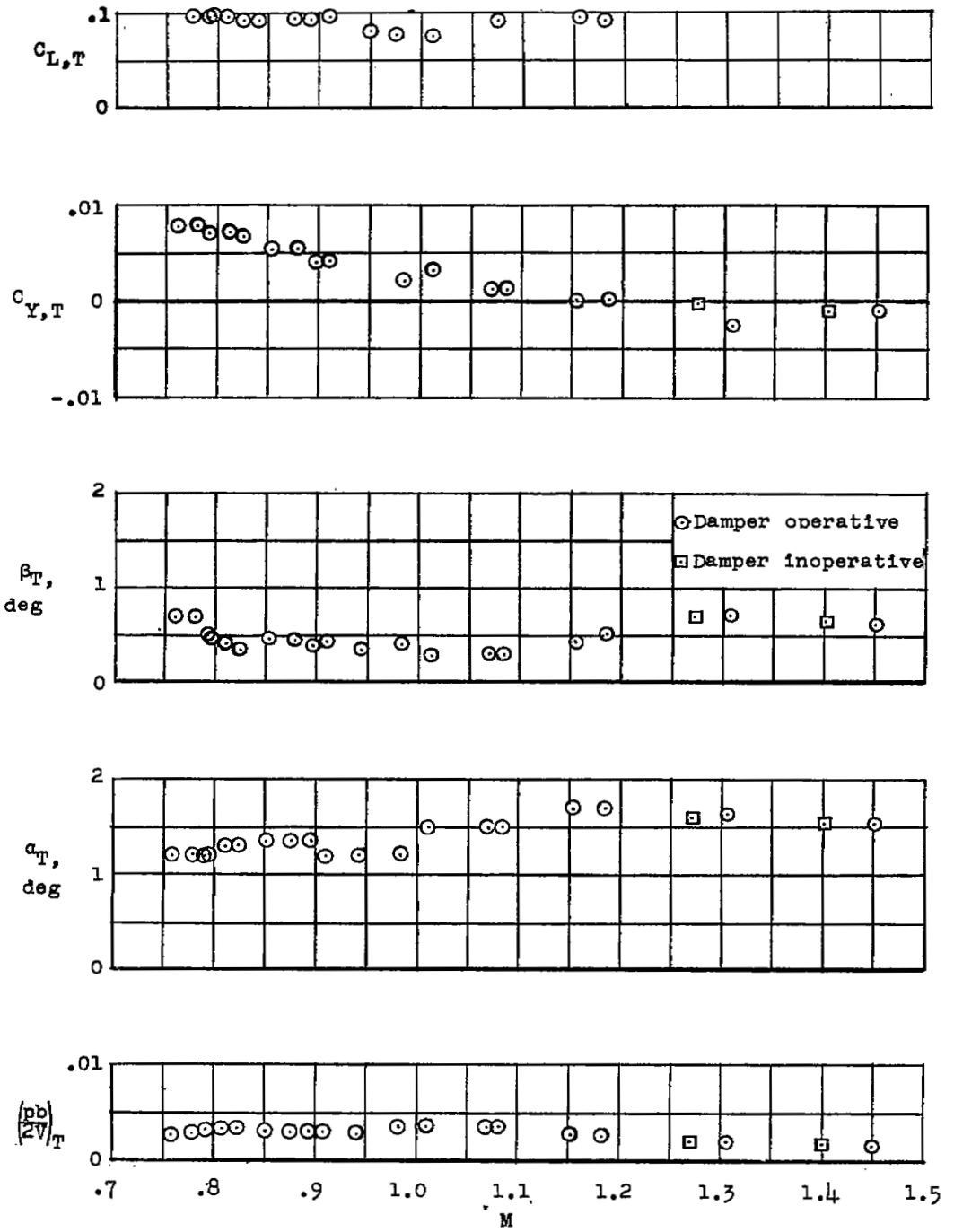

Figure 7.- Variation of model trim characteristics with Mach number.

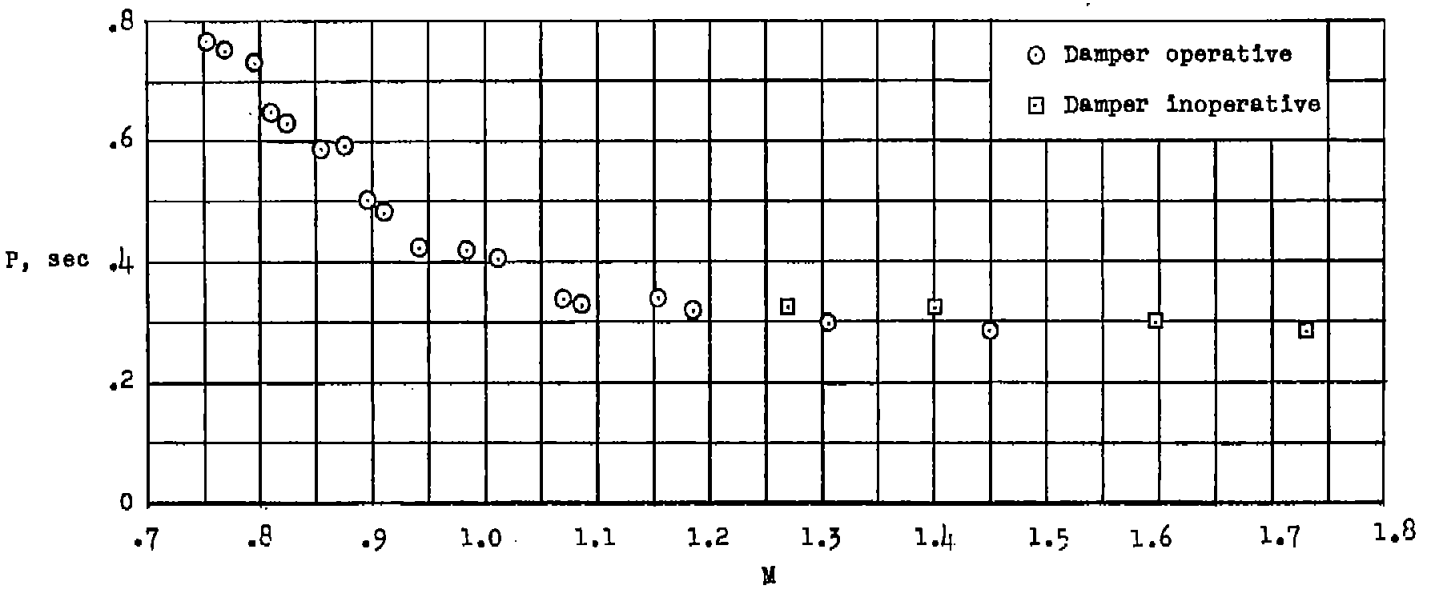

Figure 8.- Variation of the period of the lateral oscillations with Mach number. Damper inoperative and damper operative.

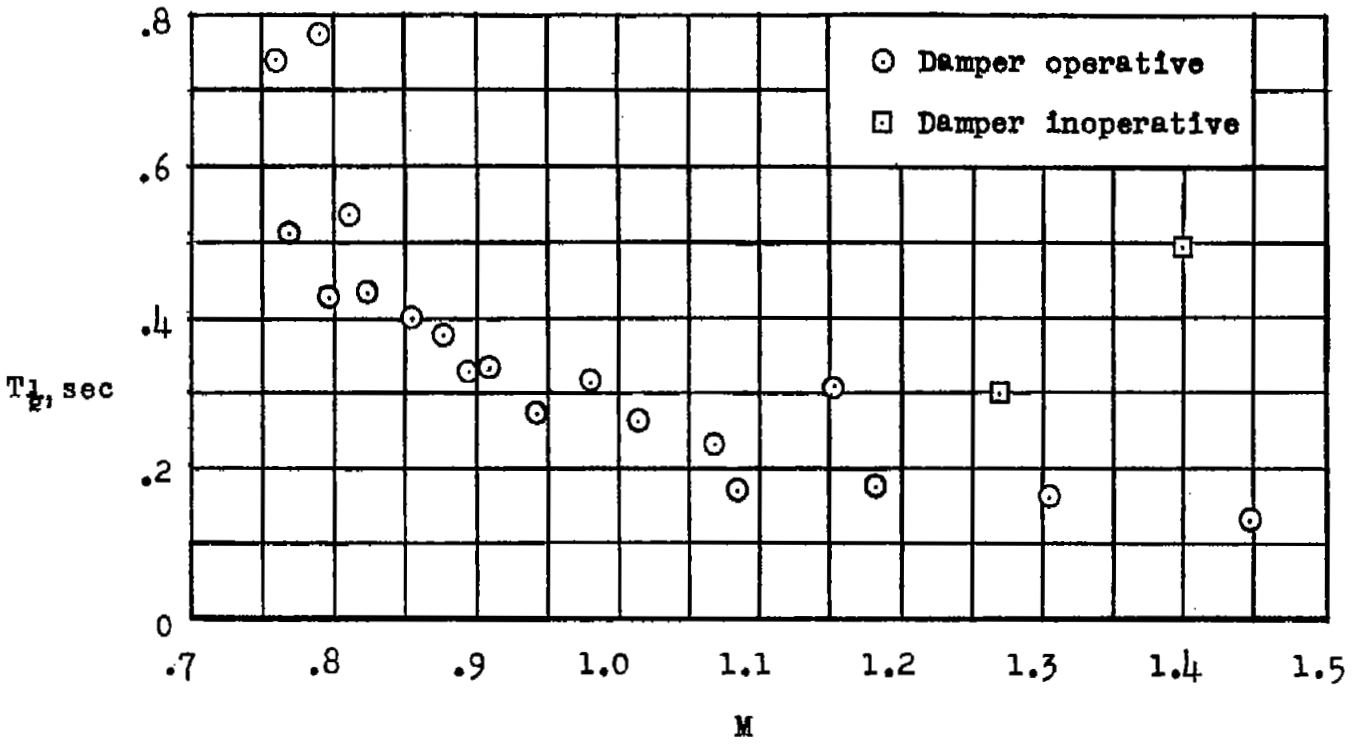

Figure 9.- Variation of the damping of the lateral oscillations with Mach number. Damper inoperative and damper operative.

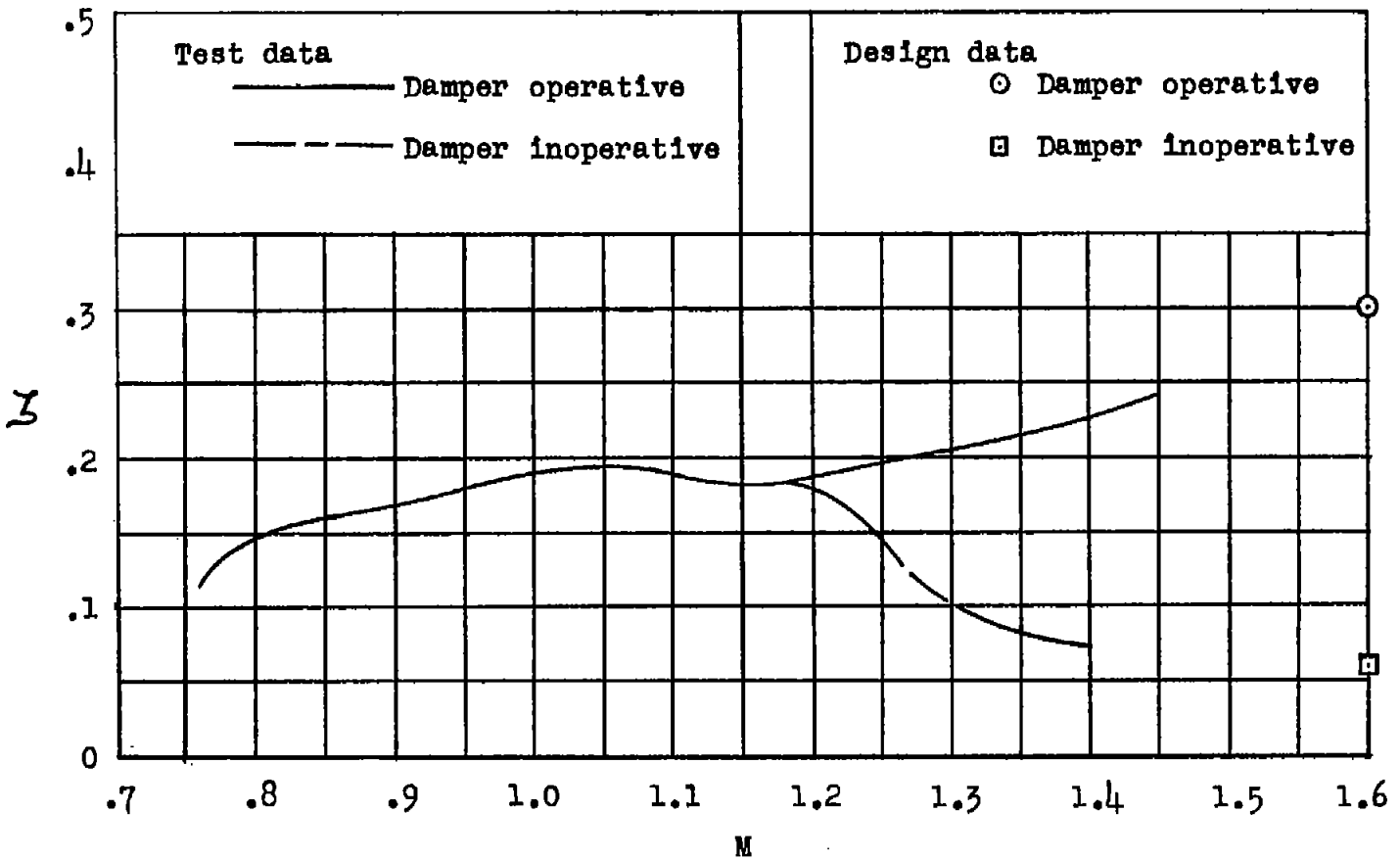

Figure 10.- Comparison of critical damping ratio. Damper inoperative and damper operative.

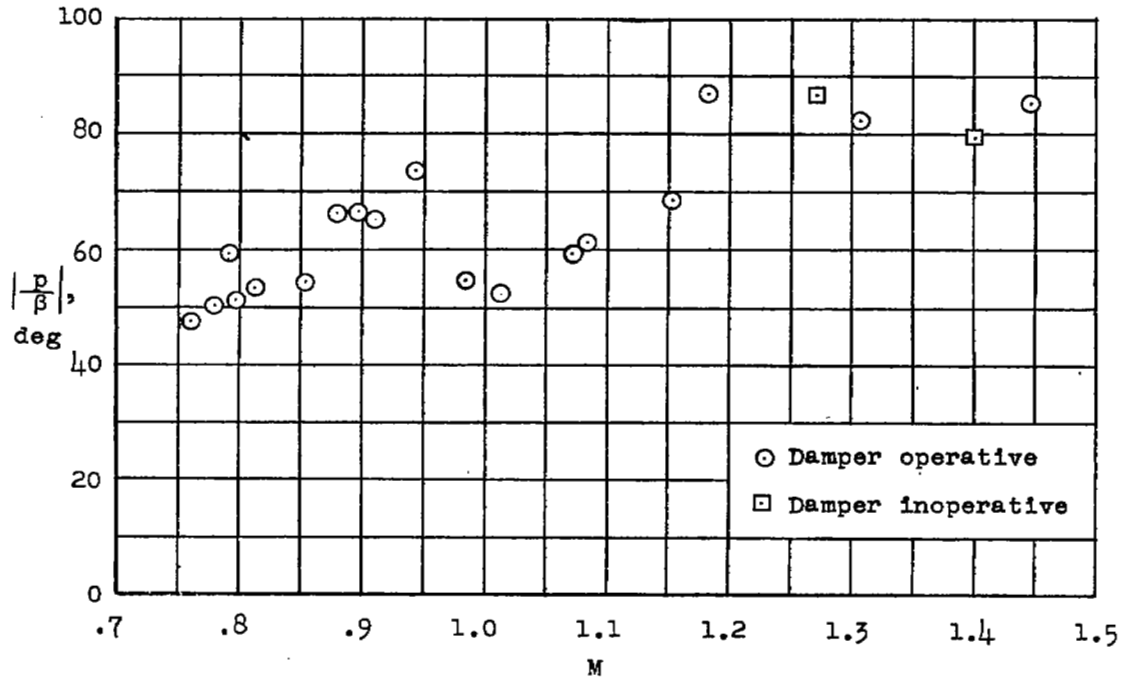

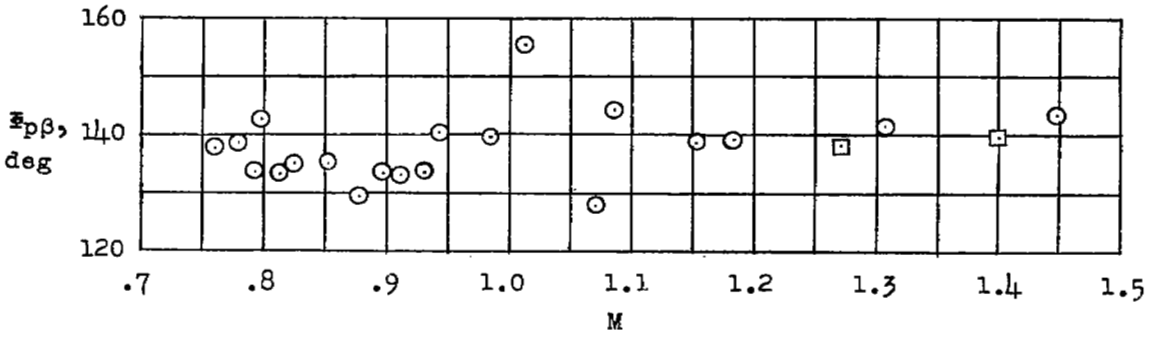

Figure 11.- Variation of amplitude ratio and phase of rolling velocity to angle of sideslip with Mach number. Damper inoperative and damper operative.

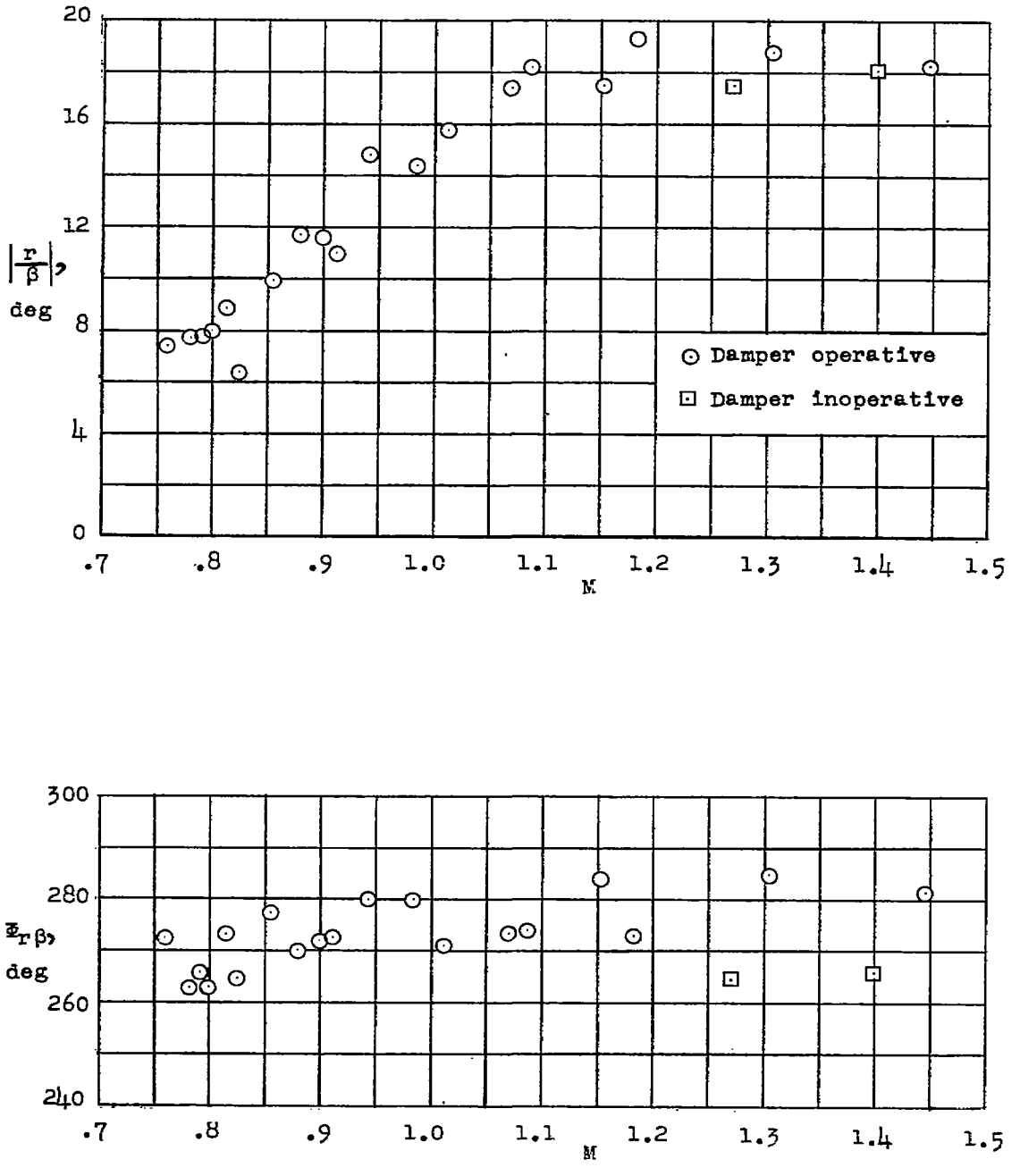

Figure 12.- Variation of amplitude ratio and phase of yawing velocity to angle of sideslip with Mach number. Damper inoperative and damper operative.

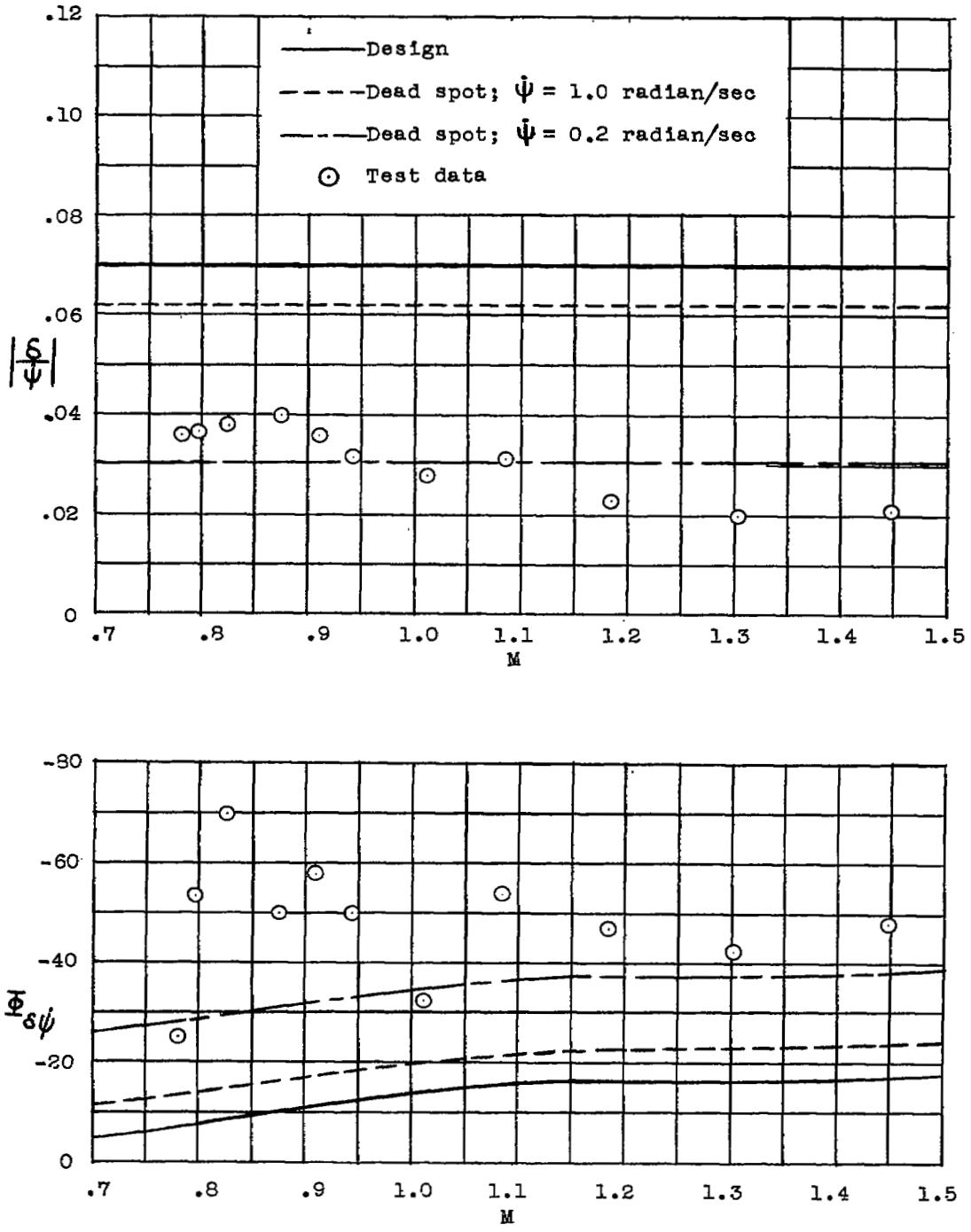

Figure 13.- Variation of gain and phase lag of yaw-rate damper system with Mach number.

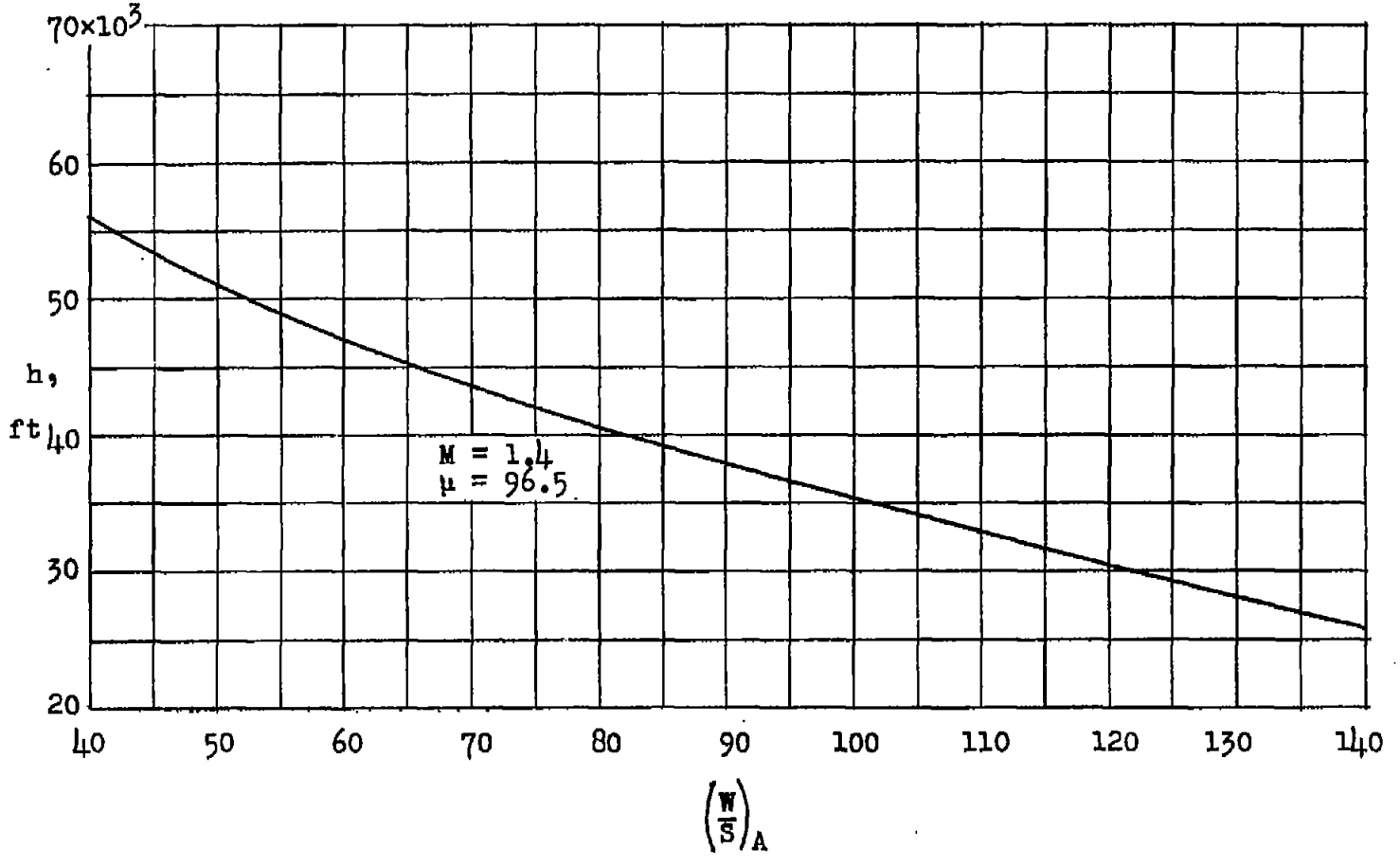

Figure 14.- Airplane flight conditions simulated by model assuming 10:1 scale factor and same relative-density factor.

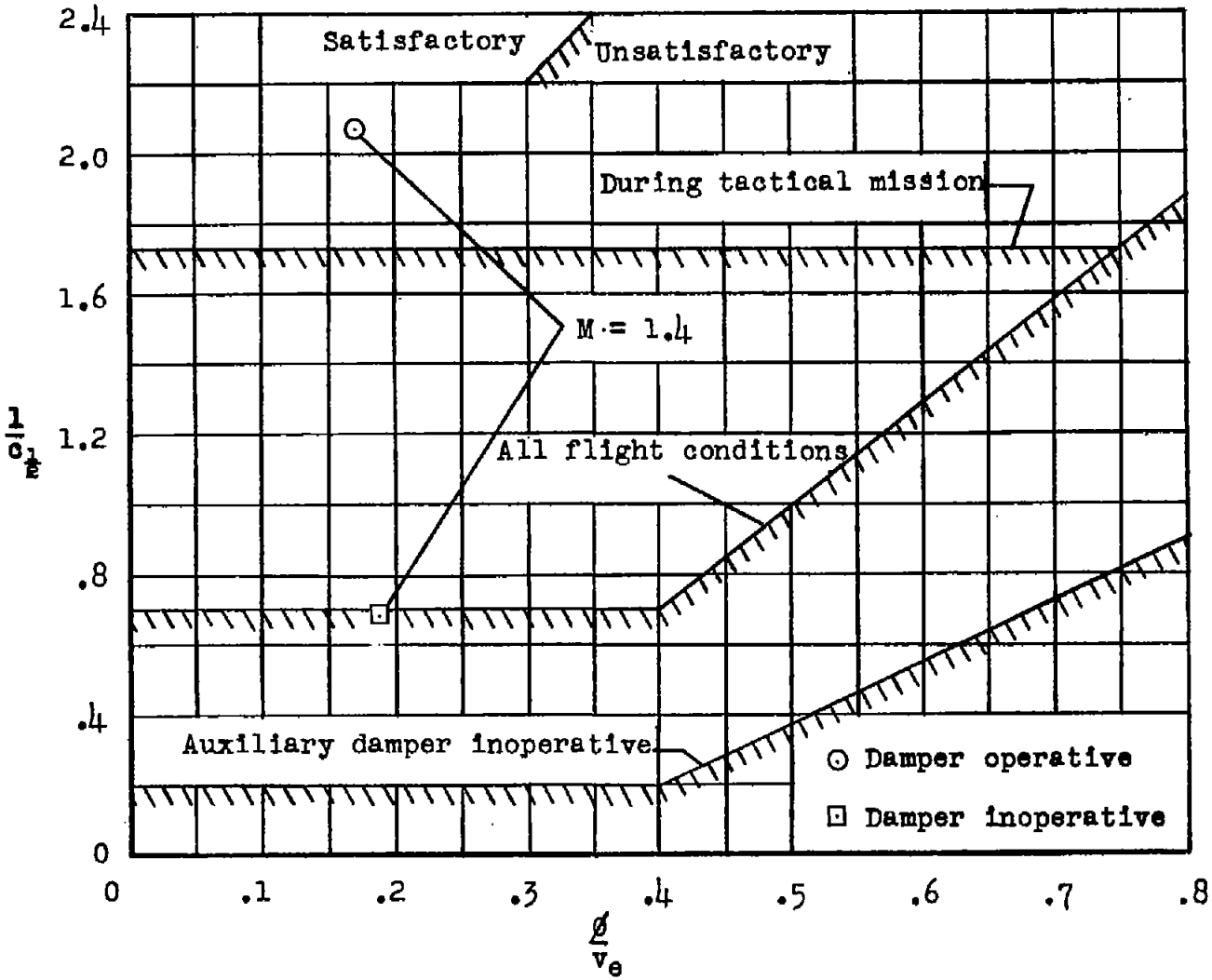

Figure 15.- Lateral-oscillation-damping requirement.

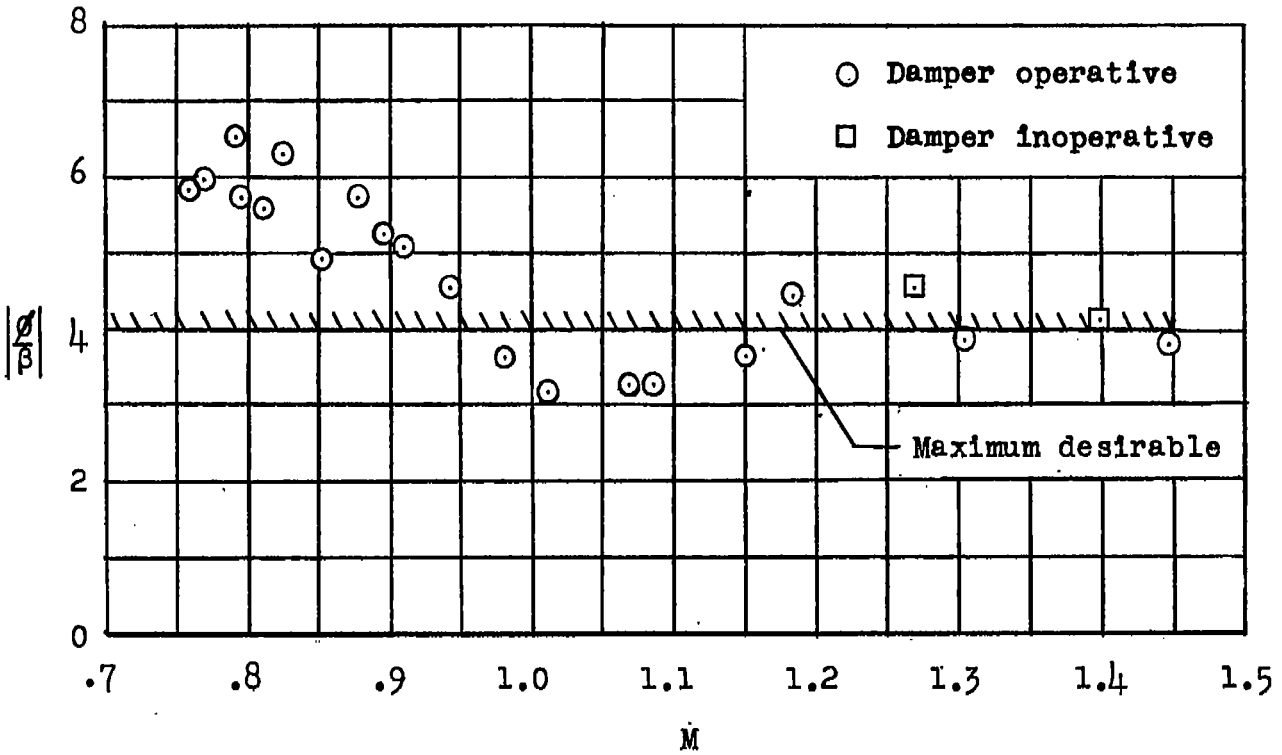

Figure 16.- Variation of roll-to-sideslip ratio with Mach number.

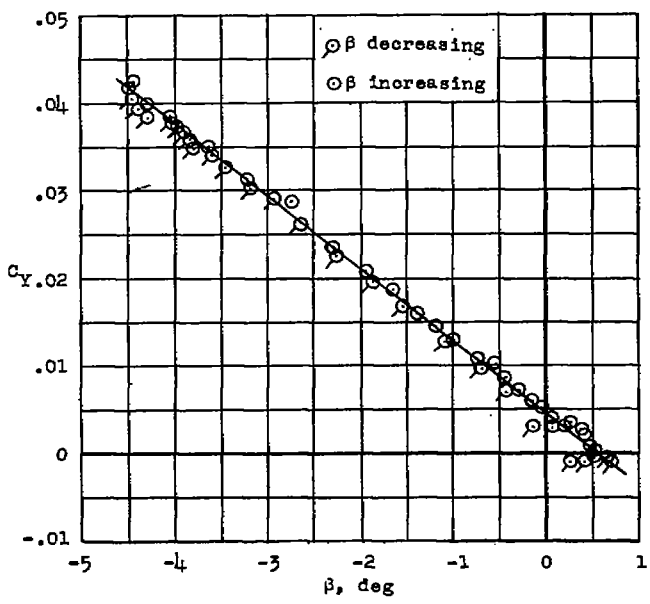

(a) M = 1.66.

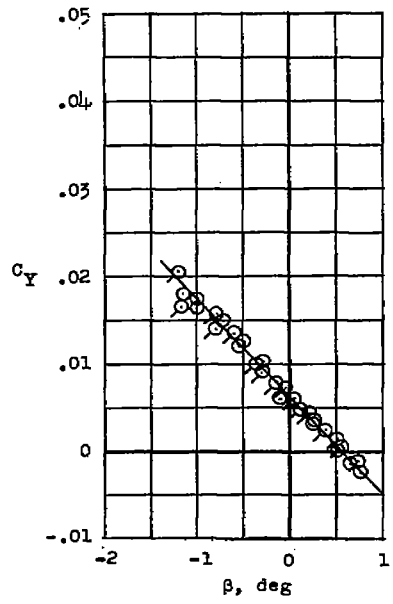

(b) M = 1.33.

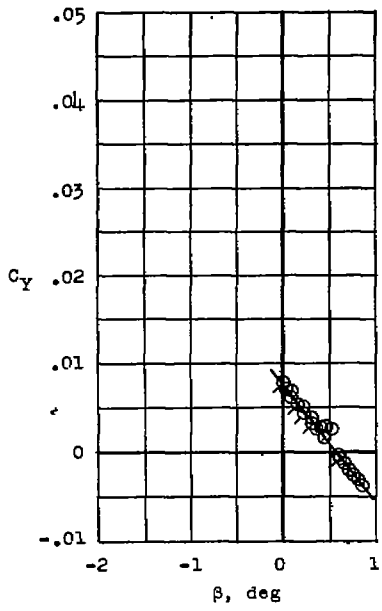

(c) M = 1.00.

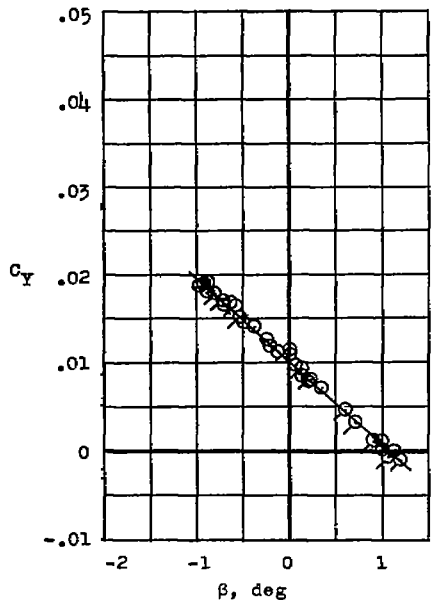

(d) M = 0.80.

Figure 17.- Typical variations of lateral-force coefficient with Mach number. Damper operative.

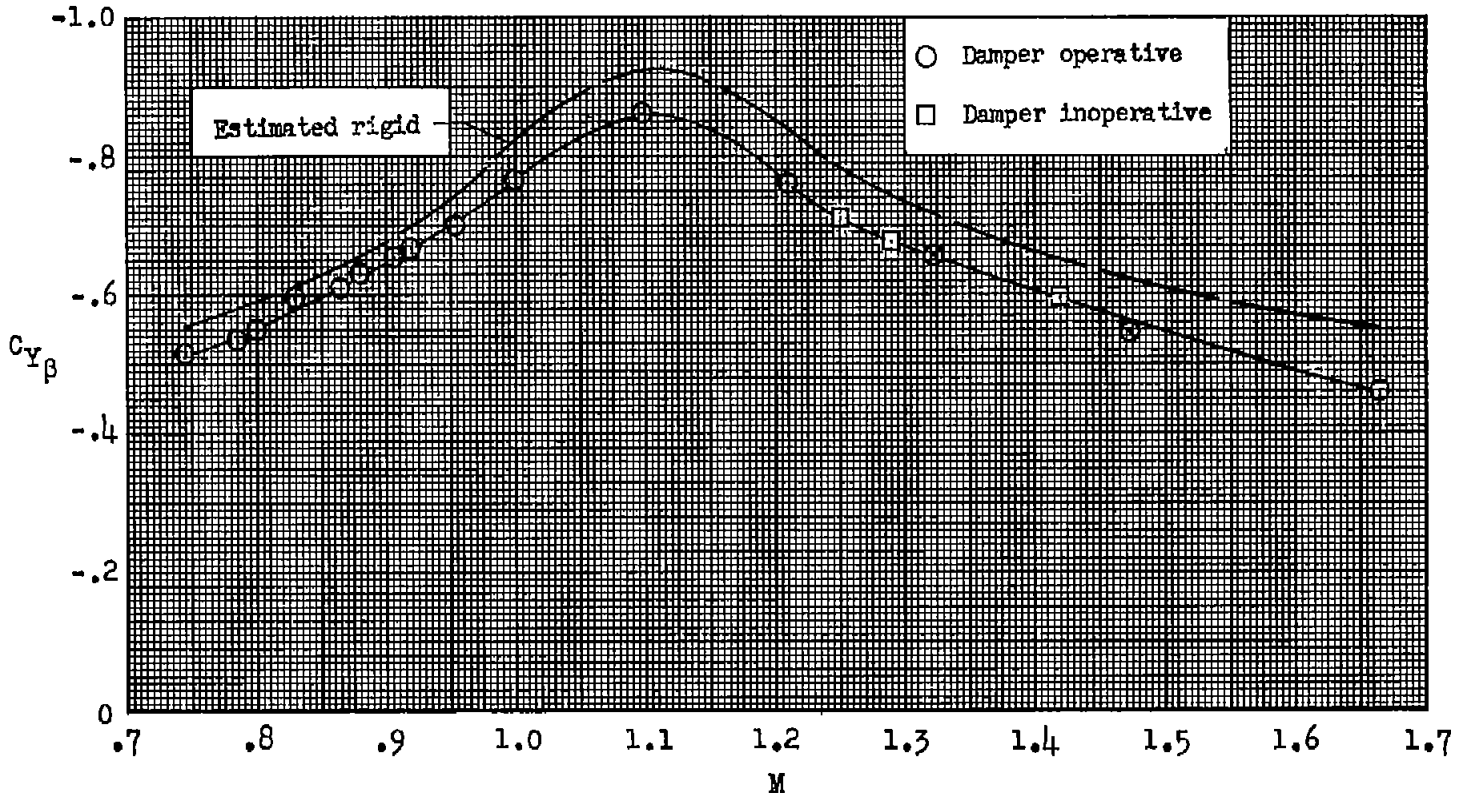

Figure 18.- Variation of lateral-force derivative with Mach number.

$$\frac{mV}{qS}\left[\left|\frac{\dot{\beta}}{\beta}\right| + \left|\frac{r}{\beta}\right| - \alpha\left|\frac{p}{\beta}\right|\right] - \left|\frac{C_Y}{\beta}\right| = 0$$

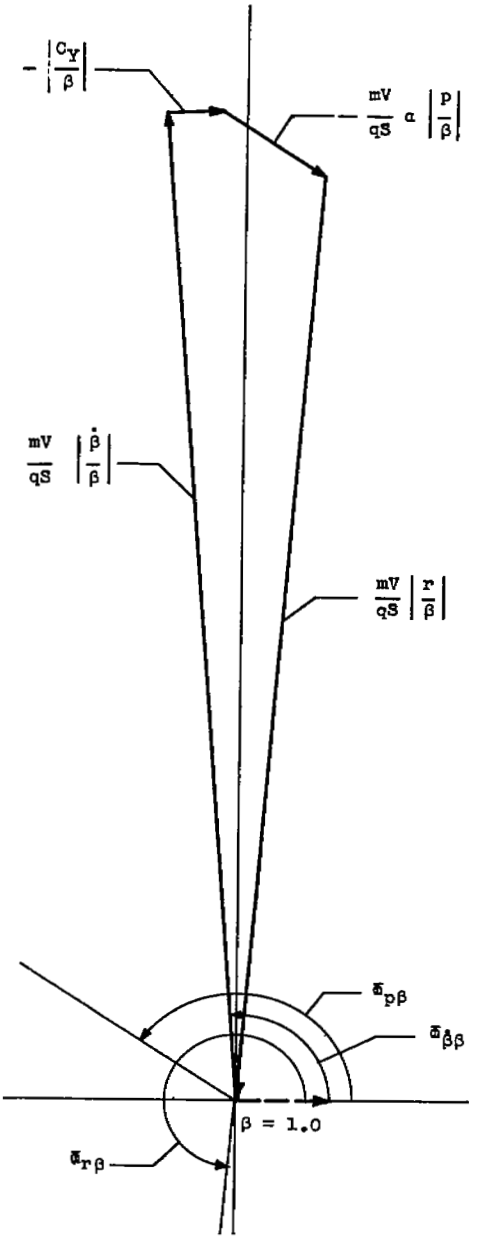

(a) Lateral-force equation.

Figure 19.- Typical time-vector plots. M = 1.40.

$$\frac{I_X}{qSb}\left|\frac{\dot{p}}{\beta}\right| - \frac{I_{XZ}}{qSb}\left|\frac{\dot{r}}{\beta}\right| - C_{l_p}\left(\frac{b}{2V}\right)\left|\frac{p}{\beta}\right| - C_{l_r}\left(\frac{b}{2V}\right)\left|\frac{r}{\beta}\right| - C_{l_\beta} = 0$$

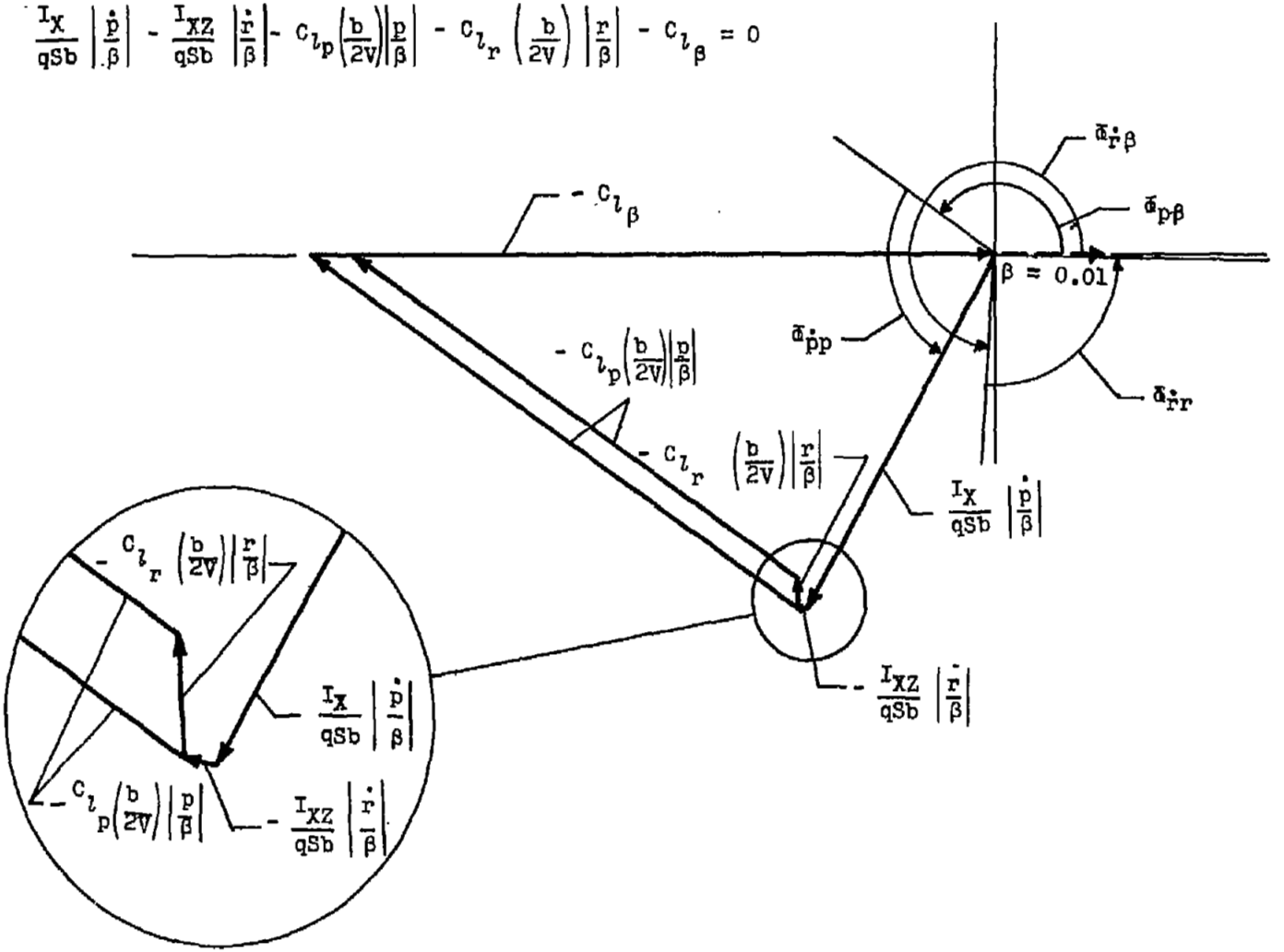

(b) Rolling-moment equation.

Figure 19.- Continued.

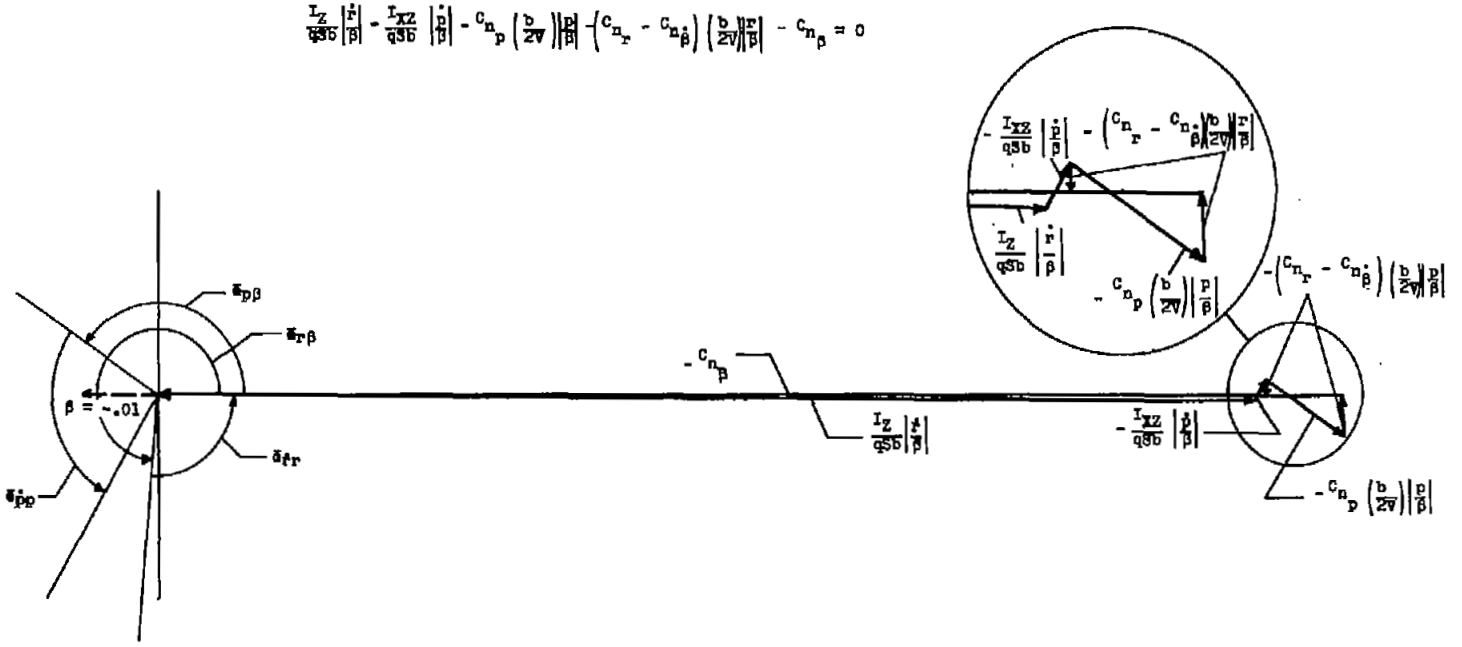

(c) Yawing-moment equation.

Figure 19.- Concluded.

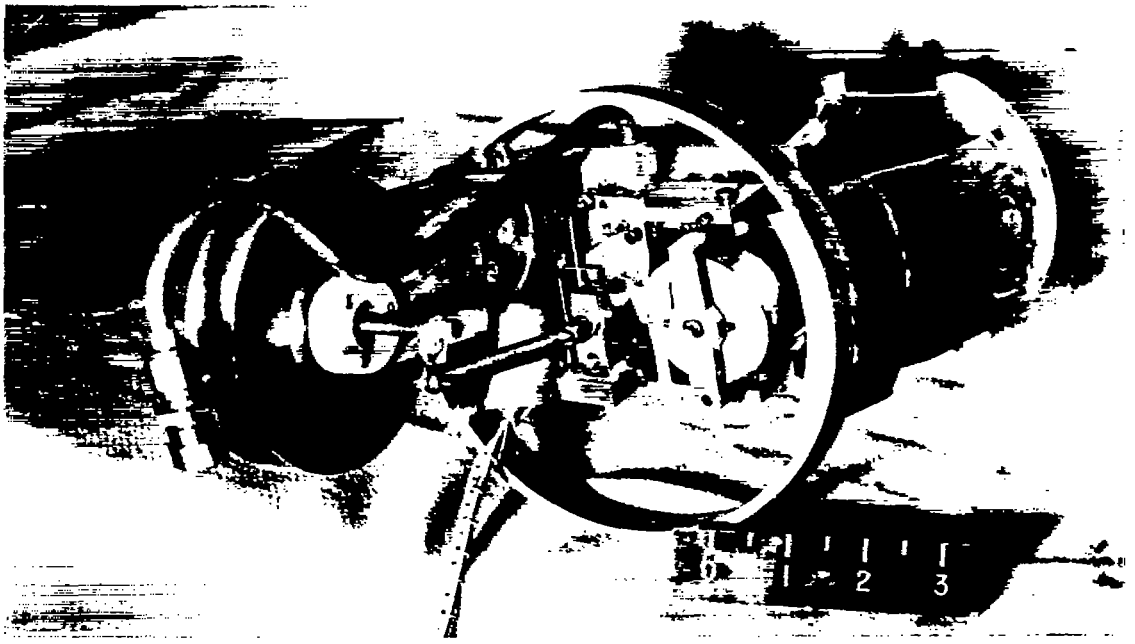

L-90455

(a) Close-up view showing damper, servo, and gyro.

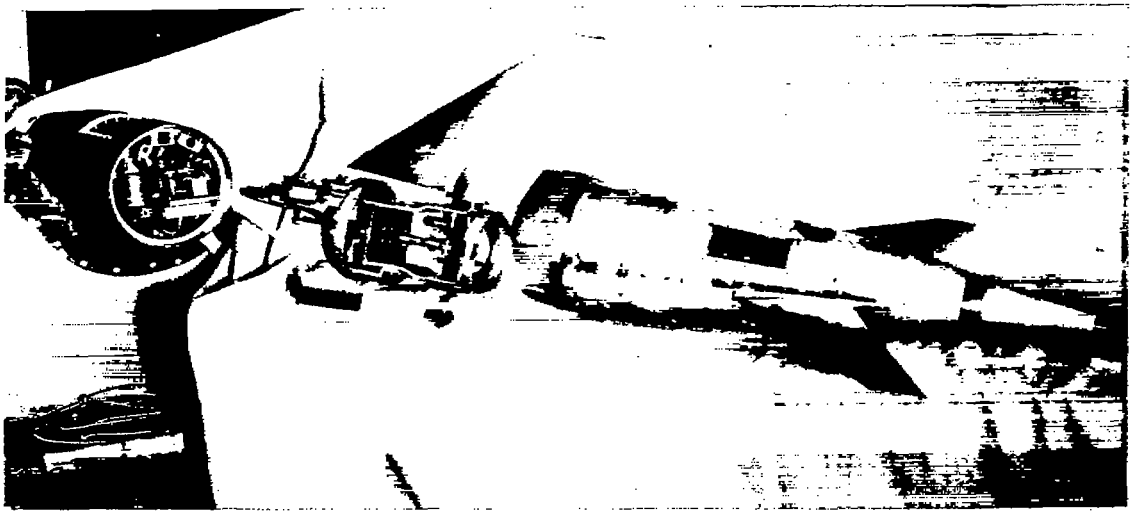

L-90454

(b) Exploded view showing system and tail section of model.

Figure 20.- Auxiliary damper system.

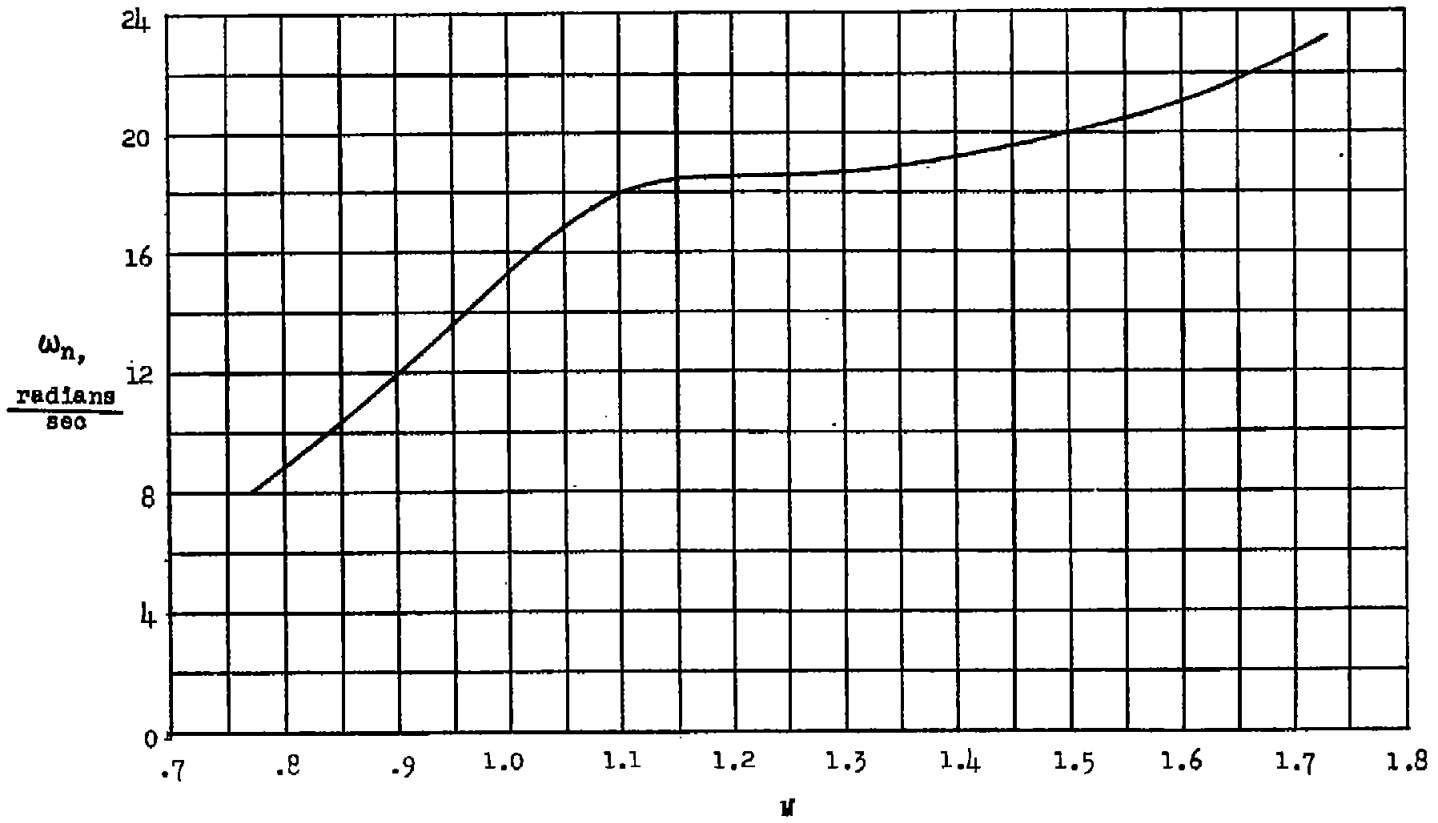

Figure 21.- Variation of model undamped natural frequency with Mach number.

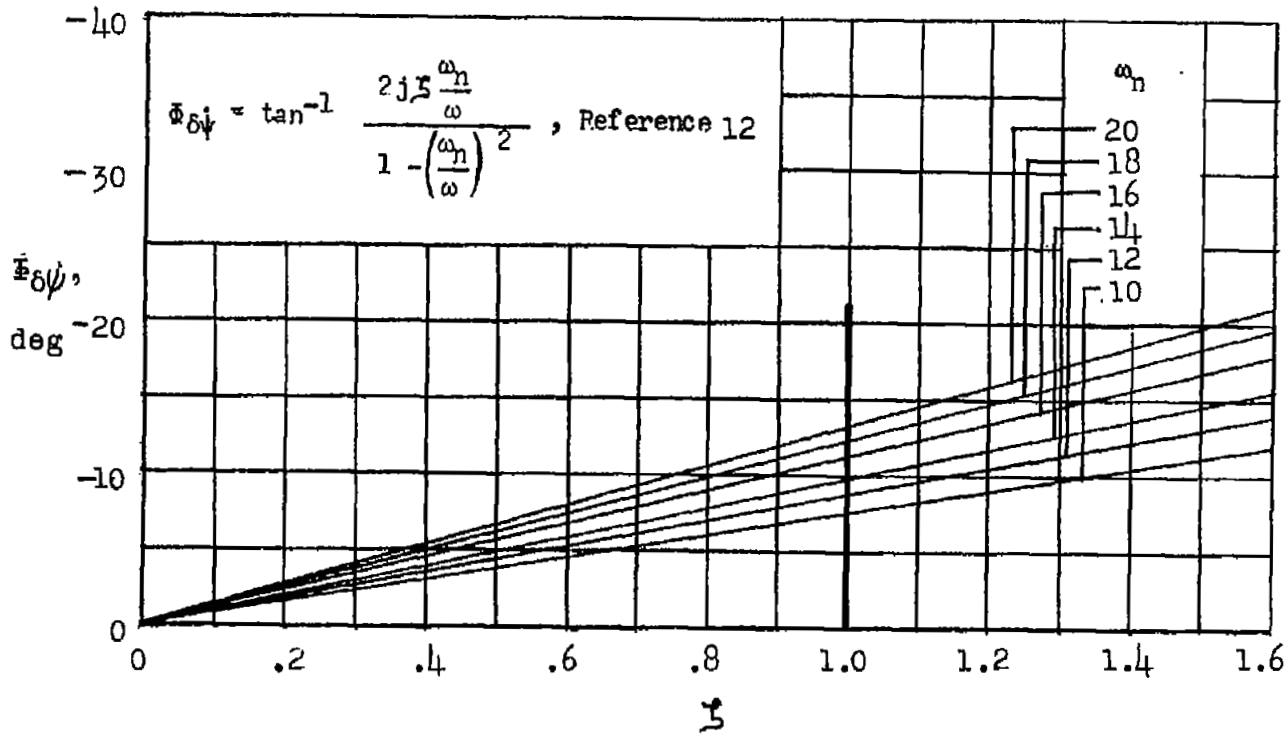

Figure 22.- Theoretical variation of phase angle with damping ratio as determined from reference 11.